A&A 668, A161 (2022)
https://doi.org/10.1051/0004-6361/202244198

Astronomy & Astrophysics

Pulsating hydrogen-deficient white dwarfs and pre-white dwarfs observed with TESS

V. Discovery of two new DBV pulsators, WDJ152738.4−450207.4 and WD 1708−871, and asteroseismology of the already known DBV stars PG 1351+489, EC 20058−5234, and EC 04207−4748

A. H. Córsico[1,2], M. Uzundag[3,4], S. O. Kepler[5], L. G. Althaus[1,2], R. Silvotti[6], P. A. Bradley[7], A. S. Baran[8], D. Koester[9], K. J. Bell[10,⋆], A. D. Romero[5], J. J. Hermes[11], and N. P. Gentile Fusillo[12]

[1] Grupo de Evo slución Estelar y Pulsaciones, Facultad de Ciencias Astronómicas y Geofísicas, Universidad Nacional de La Plata, Paseo del Bosque s/n, 1900 La Plata, Argentina
e-mail: acorsico@fcaglp.unlp.edu.ar
[2] IALP – CONICET, 1900 La Plata, Argentina
[3] Instituto de Física y Astronomía, Universidad de Valparaíso, Gran Bretaña 1111, Playa Ancha, Valparaíso 2360102, Chile
[4] European Southern Observatory, Alonso de Cordova 3107, Santiago, Chile
[5] Instituto de Física, Universidade Federal do Rio Grande do Sul, 91501-900 Porto-Alegre, RS, Brazil
[6] INAF-Osservatorio Astrofisico di Torino, strada dell'Osservatorio 20, 10025 Pino Torinese, Italy
[7] XCP-6, MS F-699 Los Alamos National Laboratory, Los Alamos 87545, USA
[8] Uniwersytet Pedagogiczny, Obserwatorium na Suhorze, ul. Podchorążych 2, 30-084 Kraków, Poland
[9] Institut für Theoretische Physik und Astrophysik, Universität Kiel, 24098 Kiel, Germany
[10] DIRAC Institute, Department of Astronomy, University of Washington, Seattle, WA 98195, USA
[11] Department of Astronomy & Institute for Astrophysical Research, Boston University, 725 Commonwealth Ave., Boston, MA 02215, USA
[12] European Southern Observatory, Karl-Schwarzschild-Straße 2, Garching 85748, Germany

Received 6 June 2022 / Accepted 7 October 2022

ABSTRACT

Context. The TESS space mission has recently demonstrated its great potential to discover new pulsating white dwarf and pre-white dwarf stars, and to detect periodicities with high precision in already known white-dwarf pulsators.
Aims. We report the discovery of two new pulsating He-rich atmosphere white dwarfs (DBVs) and present a detailed asteroseismological analysis of three already known DBV stars employing observations collected by the TESS mission along with ground-based data.
Methods. We processed and analyzed TESS observations of the three already known DBV stars PG 1351+489 (TIC 471015205), EC 20058−5234 (TIC 101622737), and EC 04207−4748 (TIC 153708460), and the two new DBV pulsators WDJ152738.4−50207.4 (TIC 150808542) and WD 1708−871 (TIC 451533898), whose variability is reported for the first time in this paper. We also carried out a detailed asteroseismological analysis using fully evolutionary DB white-dwarf models built considering the complete evolution of the progenitor stars. We constrained the stellar mass of three of these target stars by means of the observed period spacing, and derived a representative asteroseismological model using the individual periods, when possible.
Results. We extracted frequencies from the TESS light curves of these DBV stars using a standard pre-whitening procedure to derive the potential pulsation frequencies. All the oscillation frequencies that we found are associated with g-mode pulsations with periods spanning from ∼190 s to ∼936 s. We find hints of rotation from frequency triplets in some of the targets, including the two new DBVs. For three targets, we find constant period spacings, which allowed us to infer their stellar masses and constrain the harmonic degree ℓ of the modes. We also performed period-to-period fit analyses and found an asteroseismological model for three targets, with stellar masses generally compatible with the spectroscopic masses. Obtaining seismological models allowed us to estimate the seismological distances and compare them with the precise astrometric distances measured with *Gaia*. We find a good agreement between the seismic and the astrometric distances for three stars (PG 1351+489, EC 20058-5234, and WD 1708-871); although, for the other two stars (EC 04207-4748 and WD J152738.4-50207), the discrepancies are substantial.
Conclusions. The high-quality data from the TESS mission continue to provide important clues which can be used to help determine the internal structure of pulsating pre-white dwarf and white dwarf stars through the tools of asteroseismology.

Key words. asteroseismology – white dwarfs – stars: evolution – stars: interiors – methods: observational

⋆ NSF Astronomy and Astrophysics Postdoctoral Fellow, Seattle, USA

1. Introduction

Pulsating white dwarfs (WDs) and pre-WDs constitute one of the most thoroughly studied classes in the zoo of pulsating stars (see, e.g., Catelan & Smith 2015; Aerts 2021; Kurtz 2022). Their multiperiodic brightness fluctuations, with periods in the range 100−7000 s, and amplitudes up to 0.4 mag, are due to low-degree ($\ell \leq 3$) nonradial gravity (g) mode pulsations. These modes are excited by a driving mechanism related to the partial ionization of the dominant chemical species in the zone of driving, which is located at the outer regions of these stars (Winget & Kepler 2008; Fontaine & Brassard 2008; Althaus et al. 2010). The most populous class of pulsating WDs is that of the ZZ Ceti or DAV stars, which are DA-type, hydrogen (H)-rich atmospheres, at $T_{\rm eff} \sim 10\,500 - 13\,000$ K, of which ∼500 objects are known so far (Córsico et al. 2019a; Vincent et al. 2020; Guidry et al. 2021; Romero et al. 2022). At higher temperatures ($T_{\rm eff} \sim 21\,000 - 30\,000$ K), and with helium (He)-dominated atmospheres, we find the pulsating WDs called V777 Her or DBVs. Although not many DBVs are known at present (47 objects; see Córsico et al. 2019a; Duan et al. 2021; Vanderbosch et al. 2022), these compact pulsating stars are very interesting because the origin of DB WDs is not entirely clear. They are probably descendants of the PG 1159 stars (oxygen (O)-, carbon (C)-, and He-rich atmospheres) after going through the DO WD (with very hot He-rich atmospheres) stage (Dehner & Kawaler 1995; Althaus et al. 2005; Battich et al. 2020; Bédard et al. 2022). A large fraction of PG 1159 stars are believed to be the result of a born-again episode, that is, a very late thermal pulse (VLTP) experienced by a WD during its early cooling phase (Fujimoto 1977; Schoenberner 1979; Iben et al. 1983; Althaus et al. 2005). During the VLTP, most of the H content of the remnant is violently burned (Herwig et al. 1999; Miller Bertolami & Althaus 2006). As a result, the remnant is forced to evolve rapidly back to the asymptotic giant branch (AGB) and finally into the central star of a planetary nebula as a hot H-deficient object. After that, gravitational settling acting during the early stages of WD evolution causes He to float and heavier elements (C and O) to sink, giving rise to an He-dominated surface, and turning the PG 1159 star into a DO WD (Unglaub & Bues 2000), and later into a DB WD (Althaus et al. 2005). Alternatively, some DB WDs could be descendants of DO WDs resulting from evolutionary channels that do not involve only the PG 1159 stars. For instance, they could be the result of post-merger evolution involving the giant, H-deficient RCrB stars (Rauch et al. 2006; Althaus et al. 2009). Also, DB WDs could be the result of the merger of two WDs (Webbink 1984; Lauer et al. 2019).

DBV stars are found to pulsate with periods between 120 and 1080 s (Winget & Kepler 2008). Their existence was anticipated theoretically (Winget et al. 1982b) before being discovered shortly after (Winget et al. 1982a). Furthermore, g modes in DBVs are thought to be excited by a combination of the κ mechanism acting in the He partial ionization zone – and thus setting the blue edge of the DBV instability strip (Winget et al. 1983) and the "convective driving" mechanism (Brickhill 1991), which is possibly dominant once the outer convection zone has deepened enough (Van Grootel et al. 2017).

At the beginning of the exploration of pulsating WDs, the discovery of variable objects with single-site observations (e.g., Landolt 1968; Winget et al. 1982a) and even with multisite campaigns, such as those of the Whole Earth Telescope (WET; Nather et al. 1990; Winget et al. 1994), was challenging and slow. A very interesting account of those early days can be found in the article of Bradley (2021). Later on, discoveries of pulsating WDs increased enormously thanks to the identification of candidates from the Sloan Digital Sky Survey (SDSS, York et al. 2000; Kleinman et al. 2013; Kepler et al. 2015, 2016, 2019), and in recent years, with space missions. In particular, the *Kepler*/K2 mission (Borucki et al. 2010; Howell et al. 2014) resulted in the study of 32 ZZ Ceti stars and three DBV stars (Østensen et al. 2011; Bell et al. 2015, 2017; Hermes et al. 2017a,b; Córsico 2020; Duan et al. 2021). That mission ended in 2018. The Transiting Exoplanet Survey Satellite (TESS mission, Ricker et al. 2015), on the other hand, is currently in its fourth year of operation and has completed its initial 2-yr mission in 2019 and 2020 to observe ∼85% of the whole sky searching for small planets orbiting nearby stars. The mission is planned to observe 69 sectors of the sky, covering it completely. As of April 2022, the mission is observing sector 51. TESS has allowed the discovery of pulsating stars, and, in particular, pulsating WDs and pre-WDs with magnitude $G \lesssim 16$–17.

The first pulsating WD observed extensively with TESS was the DBV pulsator EC 0158−160 (TIC 257459955), which was studied and modeled in detail by Bell et al. (2019). Recently, a thorough asteroseismological analysis of the DBV star GD 358 – the archetype of the class – based on the observations gathered by the TESS mission combined with data taken from the Earth has been carried out by Córsico et al. (2022). The authors detected 26 periodicities from ∼422 s to ∼1087 s, along with eight combination frequencies with periods between ∼543 s and ∼295 s. These data, combined with a huge amount of ground-based observations (Bischoff-Kim et al. 2019), allowed Córsico et al. (2022) to find a constant period spacing of 39.25 s, compatible with a stellar mass of $M_\star = 0.581 \pm 0.031\ M_\odot$. Also, they found an asteroseismological model for GD 358 with a stellar mass of $M_\star = 0.584^{+0.025}_{-0.019}\ M_\odot$, compatible with the stellar mass derived from the period spacing, and in agreement with the spectroscopic mass ($M_\star = 0.560 \pm 0.028\ M_\odot$). The seismological distance of GD 358, $d_{\rm seis} = 42.85 \pm 0.73$ pc, is in good agreement with the precise astrometric distance measured by *Gaia* (EDR3), $d_{\rm Gaia} = 43.02 \pm 0.04$ pc.

In this work, we present new TESS observations of the already known DBV stars PG 1351+489, EC 20058−5234, and EC 04207−4748. In addition, we report for the first time the variability of the DB WDs, WDJ 152738.4−450207.4, and WD 1708−871. With the discovery of these two new DBVs, the number of known stars of this class increases to 49. We perform a detailed asteroseismological analysis of these stars on the basis of the fully evolutionary models of DB WDs computed by Althaus et al. (2009). The present study is the fifth in our series of papers devoted to the study of pulsating H-deficient WDs observed with TESS. The first article is focused on six already known GW Vir stars (Córsico et al. 2021); the second one is devoted to the discovery of two new GW Vir stars, specifically DOVs (Uzundag et al. 2021); the third paper is dedicated to the DBV star GD 358 (Córsico et al. 2022); and the fourth one is focused on the discovery of two additional GW Vir stars (Uzundag et al. 2022).

The paper is organized as follows. In Sect. 2 we provide a brief account of the main characteristics of the studied DB stars. In Sect. 3, we describe the methods we applied to obtain the pulsation periods of each target star. A brief summary of the stellar models of DB WD stars employed for the asteroseismological analysis of these stars is provided in Sect. 4. Section 5 is devoted to the asteroseismological modeling of the target stars, including the search for a constant period spacing in the sets of periods of each star by applying statistical tests, assessing the stellar mass of each object through the use of the period spacing when

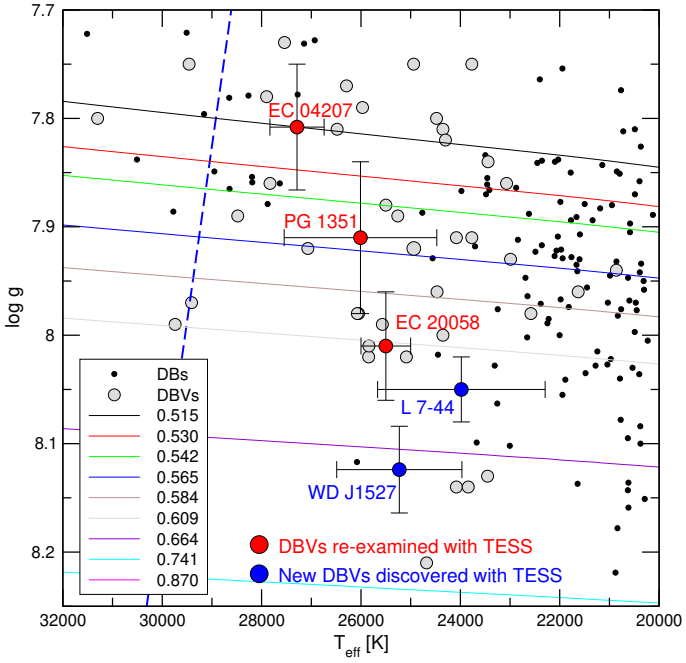

Fig. 1. Location of DB WDs in the $T_{\rm eff}-\log g$ diagram (Kepler et al. 2019), marked with small black circles. Also depicted is the location of the published DBV stars (gray circles), according to the compilation by Córsico et al. (2019a) and including also the newly discovered DBV stars by Duan et al. (2021) and Vanderbosch et al. (2022). The target stars of the present paper are highlighted with red circles corresponding to three already known DBVs, and with blue circles associated with the two new DBVs observed with TESS and reported here for the first time. The DB WD evolutionary tracks of Althaus et al. (2009) are displayed with different colors according to the stellar-mass values (in solar units). The blue-dashed line represents the theoretical dipole ($\ell = 1$) blue edge of the DBV instability strip, according to Córsico et al. (2009).

possible, and performing period-to-period fits with the aim of finding an asteroseismological model for each DBV star. Finally, in Sect. 6, we summarize our main results and make some concluding remarks.

2. The target stars

In this study, we announce the discovery of two new DBVs, WD J152738.4−450207.4, and WD 1708−871 (L 7−44), and also report new TESS observations of the already known DBV stars PG 1351+489, EC 20058−5234, and EC 04207−4748. The location of the five stars in the $\log T_{\rm eff}$ versus $\log g$ diagram is displayed in Fig. 1. These stars were classified as WD candidates with a a probability of being a WD $P_{\rm WD} \geq 0.99$ by Gentile Fusillo et al. (2019) based on their colors and *Gaia* DR2 parallaxes. The *Gaia* EDR3 parallaxes and corresponding distances are given in Table 1 from Bailer-Jones et al. (2021). We also describe the basic characteristics of these stars below and summarize their stellar properties in Table 1.

PG 1351+489 (hereafter PG 1351; also known as TIC 471015205, V*EM UMa) is an known DBV star discovered by Winget et al. (1987). Since the beginning, it was realized that it could be a candidate for the first measurement of a rate of period change in a DBV star, because its power spectrum is dominated by a single high-amplitude pulsation mode with a period at ∼489 s. This star was reanalyzed by Redaelli et al. (2011), providing more precise periods and also an additional low-amplitude mode. More importantly, it was possible to obtain, for the first time for a DBV star, an estimate of the rate of period change for the period at ∼489 s of $\dot{\Pi} = (2.0 \pm 0.9) \times 10^{-13}$ s/s (Redaelli et al. 2011). Regarding the effective temperature and gravity of PG 1351, there are several spectroscopic determinations for this star. The first detailed analysis Beauchamp et al. (1999) provided $T_{\rm eff} = 22\,600 \pm 700$ K, $\log g = 7.90 \pm 0.03$ using pure He atmospheres, and $T_{\rm eff} = 26\,100 \pm 700$ K, $\log g = 7.89 \pm 0.03$ employing atmospheres with impurities of H. The analysis of Bergeron et al. (2011) indicates that $T_{\rm eff} = 26\,010 \pm 1536$ K, $\log g = 7.91 \pm 0.07$ (see Fig. 1), obtained by assuming H contamination ($\log {\rm H/He} = -4.37 \pm 0.82$). Koester & Kepler (2015) estimate $T_{\rm eff} = 28434 \pm 124$, $\log g = 7.89 \pm 0.02$, $\log {\rm H/He} < -3.1$, and $\log {\rm Ca/He} < -4.0$. PG 1351 has been asteroseismologically modeled by Córsico et al. (2014), and were able to place constraints on the neutrino magnetic dipole moment. The star has also been used to infer bounds to the axion mass by Battich et al. (2016).

EC 20058−5234, also known as QU Tel (henceforth EC 20058; also known as TIC 101622737) is an already known DBV star whose variability was reported by Koen et al. (1995), who found that the pulsation spectrum appeared to be stable. This star was long scrutinized by Sullivan (2003, 2005), and Sullivan et al. (2007, 2008, 2017). In particular, Sullivan et al. (2008) increased the number of detected frequencies and performed an asteroseismic global-model analysis. Interestingly, these authors found that EC 20058 had very stable pulsation periods, which meant that, in principle, it could be possible to measure the rate of period change to place constraints on the plasma neutrino emission rate (Winget et al. 2004; Dalessio et al. 2010). However, Dalessio et al. (2013) found that the pulsation frequencies of this star undergoes secular changes that are inconsistent with simple neutrino plus photon-cooling models. A detailed asteroseismological analysis of EC 20058 was carried out by Bischoff-Kim & Metcalfe (2011) to place constraints on helium diffusion in WD envelopes. The effective temperature and gravity of EC 20058 are $T_{\rm eff} = 25\,500 \pm 500$ K and $\log g = 8.01 \pm 0.05$ (Koester et al. 2014) with H and C impurities.

EC 04207−4748 (hereafter EC 04207; also known as TIC 153708460) is an already known DBV WD whose variability was discovered by Kilkenny et al. (2009), who found a pulsation spectrum dominated by a period of ∼447 s. The star was reobserved by Chote et al. (2013) who found at least four independent eigenmodes in the star, with the dominant mode having a period of ∼447 s. The light curve exhibits distinct nonsinusoidal shapes, which results in significant harmonics of the dominant frequency appearing in the Fourier transforms. The effective temperature and gravity of EC 04207 are $T_{\rm eff} = 27\,288 \pm 545$ K and $\log g = 7.808 \pm 0.058$, respectively (Voss et al. 2007). However, Koester et al. (2014) quote $T_{\rm eff} = 25\,970$ K and $\log g = 7.79$, with log H/He of −5.0.

WD J152738.4−450207.4 (hereafter WD J1527; also known as TIC 150808542) is a new DB WD star. We observed WD J1527 with the Southern Astrophysical Research (SOAR) Telescope, a 4.1-meter aperture optical and near-infrared telescope (Clemens et al. 2004), situated at Cerro Pachón, Chile. The Goodman spectrograph with a setup of 400 l/mm grating with the blaze wavelength 5500 Å (M1: 3000–7050 Å) with a slit of 1 arcsec was used. The signal-to-noise ratio (S/N) of the final spectrum is ∼150 at 4250 Å. The atmospheric parameters for WD J1527 are derived by fitting synthetic spectra to the newly obtained low-resolution spectra as described by Koester (2010). The reduced spectrum is shown in Fig. 2 with blue line and the model fits is shown with red line. WD J1527 has

Table 1. List of six DBV (V777 Her) stars studied in this work.

TIC	Name	$T_{\rm eff}$ [K]	$\log g$ [cgs]	π [mas]	d [pc]
471015205	PG 1351+489	$26\,010 \pm 1536^{(a)}$	$7.91 \pm 0.07^{(a)}$	$5.69^{+0.05}_{-0.05}$	$175.73^{+1.53}_{-1.58}$
101622737	EC 20058−5234	$25\,500 \pm 500^{(b)}$	$8.01 \pm 0.05^{(b)}$	$8.48^{+0.05}_{-0.05}$	$117.95^{+0.68}_{-0.75}$
153708460	EC 04207−4748	$27\,288 \pm 545^{(c)}$	$7.808 \pm 0.058^{(c)}$	$10.93^{+0.03}_{-0.03}$	$91.48^{+0.22}_{-0.23}$
150808542	WDJ 152738.4−450207.4	$25\,228 \pm 630^{(d)}$	$8.124 \pm 0.010^{(d)}$	$10.57^{+0.04}_{-0.04}$	$94.62^{+0.34}_{-0.37}$
451533898	L 7−44=WD 1708-891	$23\,980 \pm 1686^{(e)}$	$8.05 \pm 0.03^{(e)}$	$14.47^{+0.02}_{-0.03}$	$69.09^{+0.14}_{-0.12}$

Notes. Columns 1, 2, 3, 4, 5, and 6 correspond to the TESS input catalog number, name of the object, effective temperature, surface gravity, parallax, and distance, respectively. For details, see the text.
References. (a) Bergeron et al. (2011); (b) Koester et al. (2014); (c) Voss et al. (2007); (d) This work; (e) Rolland et al. (2018).

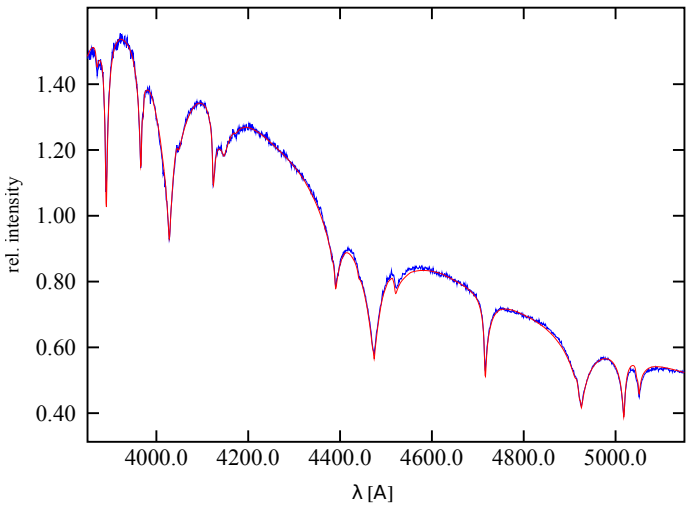

Fig. 2. Optical spectra from SOAR (blue line) of the new DBV WD J1527. Overplotted is the best-fit model atmosphere solution (red line).

$T_{\rm eff} = 25\,228 \pm 630$ K and $\log g = 8.124 \pm 0.010$, with minor H contamination. At that effective temperature, the star is well within the DBV instability strip (Fig. 1). Pulsations with periods between 229 and 1170 s are confirmed by observation in TESS sectors 12 and 38.

WD 1708−871 (hereafter L 7−44; also known as TIC 451533898) is a DB WD star characterized by $T_{\rm eff} = 23\,980 \pm 1686$ K and $\log g = 8.05 \pm 0.03$ (Rolland et al. 2018) and only an upper limit for possible H contamination. Observations in sectors 12, 13, and 39 of TESS show luminosity variations with periods in the range 466 − 937 s. The location of this star in the $T_{\rm eff} - \log g$ diagram is displayed in Fig. 1.

3. TESS data: Observations, data reduction, and analysis

Our analysis is based on 2-min short-cadence (SC) TESS data for all targets, or 20-s ultra-short-cadence when available. We used the presearch data conditioned simple aperture photometry (PDCSAP) data (Jenkins et al. 2016) downloaded from the "Barbara A. Mikulski Archive for Space Telescopes" (MAST)[1]. We extracted times in Barycentric corrected Julian days ("BJD – 245700"), and fluxes ("PDCSAP FLUX") by using the Python package `lightkurve` (Lightkurve Collaboration 2018). Afterwards, we removed outliers by applying a running 5σ clipping mask. The fluxes were normalized and transformed to amplitudes in parts-per-thousand (ppt) units. We also detrend the light curves applying a Savitzky–Golay filter with a three-day window length to remove any additional low-frequency systematic. The target pixel files (TPFs) are examined to estimate the amount of contamination from nearby unresolved targets. We have checked the contamination by looking at the `CROWDSAP` parameter, which is the ratio between target flux and total flux in the aperture. If the `CROWDSAP` is significant (<0.5), then we used *Gaia* EDR3 parallaxes to look at the contaminant targets in the field of view. Severe contamination affects the average noise level in Fourier space and thus affects also the false-alarm probability (FAP) thresholds as described in Bognár et al. (2020). After creating the final light curves, we calculated their Fourier transforms (FTs) to search for periodic signals. The detection thresholds were defined as 0.1% FAP significance level so that there is a 0.1% chance that the peaks are caused by the noise fluctuations. 0.1% FAP thresholds were calculated by randomization of the data 1000 times, as described in Kepler (1993; see Baran & Koen 2021). We identified frequency, amplitude and phase of each pulsation mode using a nonlinear least square (NLLS) method. Also, we computed sliding FTs to inspect the temporal evolution of the detected frequencies. To calculate the sliding FTs, we use a 6-day sliding window with a 2-day step size. We then compute the Fourier transform for each subset and trail them in time. In Table 2 we list the six DBV stars studied in this paper from TESS observations, including observed sectors, TESS magnitude along with name of the targets, the date and length of the runs.

3.1. PG 1351+489

PG 1351+489 ($T_{\rm mag} = 16.7$) was observed in short cadence (SC, 120s exposures) mode during sector 16 between September 11 and October 07, 2019, for 23.04 days. PG 1351 was also observed during sectors 22 and 23 (2020-Feb-18 to 2020-Apr-16) in SC, providing another 54.74 days of observations. It was also observed in fast cadence (20 s exposures) in sectors 49 and 50 (2022-Feb-26 to 2022-Apr-22), 51.11 days of observations. We examined the field of view (FOV) of PG 1351 and saw that there is a bright star that is 1.44 arcsec away from PG 1351 in sector 16. The problem is that the nearby star is about 2.4 mag brighter than PG 1351, dominating the pixels. The `CROWDSAP` parameter is around 0.3, meaning that only 30 percent of the light is coming from PG 1351, affecting the average noise level of the FT, as shown in Table 2. Including all sectors, PG 1351 was observed

[1] http://archive.stsci.edu

Table 2. Five DBV (V777 Her) stars reported in this paper from TESS observations, including the name of the targets, the TESS magnitudes, the observed sectors, and the date and length of the runs (Cols. 1–6).

TIC	Name	$T_{\rm mag}$	Obs. Sector	Start time (BJD-2 457 000)	Run length [d]	Resolution μHz	Average noise Level [ppt]	0.1% FAP [ppt]
471015205	PG 1351+489	17	16, 22, 23, 49, 50	1738.6492	128.89	0.1	1.32	6.3
101622737	EC 20058−5234	16	13, 27	1653.9251	52.74	0.22	0.66	2.54
153708460	EC 04207−4748	15	4, 5, 30, 31, 32	1410.9047	137.48	0.08	0.42	1.79
150808542	WDJ152738.4–450207.4	16	12 ,38	1627.6494	25.24	0.45	4.90	20.7
451533898	L 7−44	15	12, 13, 39	1624.9589	84.40	0.14	0.28	1.39

Notes. After Fourier transform, three different set of parameters resolution, average noise level of amplitude spectra, and detection threshold, which is defined as 0.1% false-alarm probability (FAP), are presented in Cols. 7–9, respectively.

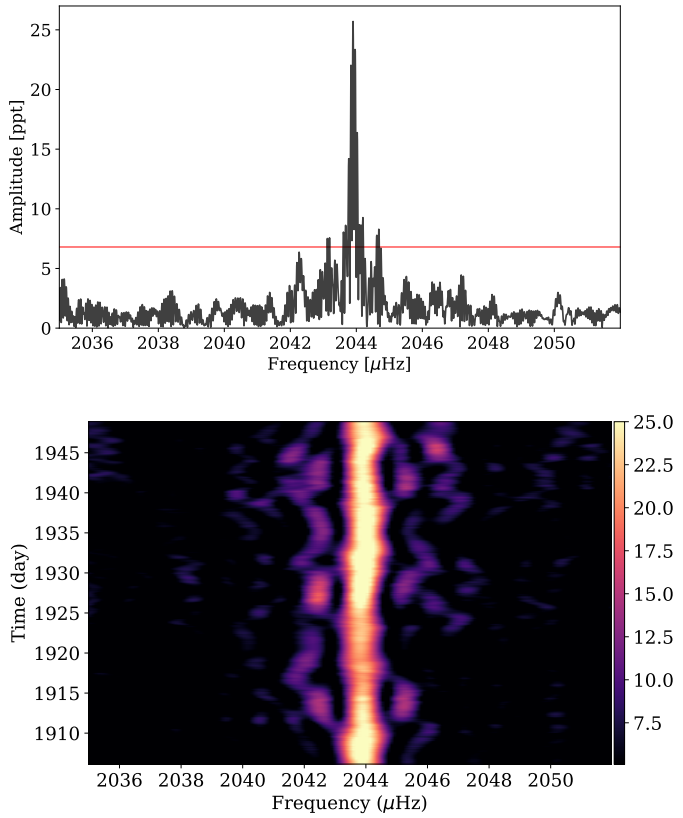

Fig. 3. *Top*: Main pulsational mode in PG 1351 presented in Table 3. Fourier transform of data taken in sector 16, 22 and 23. The red dashed line denotes the 0.1% FAP. *Bottom*: Sliding Fourier transform sectors 22 and 23 of PG 1351+489 concentrating the main pulsational mode. The color-scale illustrates amplitude in ppt units.

for 128.89 days in total. From these observations of PG 1351, we extracted only two periodicities from the light curve. The main pulsation frequency at 2043.9 μHz is present in all sectors with $S/N \geq 19$. In Fig. 3, we present the temporal FT (upper panel) and sFT (bottom panel) for 2043.9 μHz. The other peak at 4087.8 μHz, which has a lower S/N of about 5.75, is a combination frequency (often called the first harmonic, 2×2043.9 μHz). These two identified frequencies are listed in Table 3.

3.2. EC 20058−5234

EC 20058−5234 was observed in sector 13 (2019-Jun-19 to 2019-Jul-18) in camera 2. It was also observed in sector 27 (2020-Jul-04 to 2020-Jul-30) in camera 2. Sector 13 contains

Table 3. Identified frequencies and combination frequencies, periods, amplitudes (and their uncertainties) and the signal-to-noise ratio in the data of PG 1351.

Peak	ν (μHz)	Π (s)	A (ppt)	S/N
f_1	2043.901 (20)	489.260(22)	25.78(1.05)	19.8
$2f_1$	4087.802(87)	244.630(22)	6.57(1.05)	5.1

19582 measurements that span 28.4 days, while sector 27 includes 16745 measurements that span 24.3 days. There are two stars within 5 arcsec with brightnesses of 15.7 mag and 16.4 mag close to EC 20058. These two stars have only a modest effect on the noise level of the FT. The FT average noise level of sector 27 is 0.61 ppt, while it is 0.66 ppt in sector 13. We first examined the Fourier transform from each sector. Sector 13 shows two frequencies at 3558 and 3893 μHz, which are above the 0.1% FAP of 2.54 ppt. These two peaks are also present in sector 27 above the 0.1% FAP of 2.3 ppt. We also examined the FT of both sectors together, as shown in Fig. 4. These two detected frequencies are given in Table 4. This target is known to have significant phase and amplitude variations. The sliding Fourier Transform of two reported frequencies was calculated. However, the signal-to-noise ratio is insufficient to show and assess these substantial variations.

3.3. EC 04207−4748

EC 04207 was first observed in SC during cycle 1 in sector 4 and 5 (2018-Oct-18 to 2018-Dec-11). Since in sectors 4 the scatter is much higher between 1422.61 d and 1423.51 d, and between 1436.60 d and 1436.82 d, we removed these regions. Then, we added sector 5 and calculated the Fourier transform of 53 days of data detecting five independent frequencies above 0.1% FAP confidence level, which corresponds to 1.79 ppt (Fig. 5 top). The FT median noise level is 0.39 ppt. The S/N of the detected frequencies ranges from 5 to 69. EC 04207 was also observed during three consecutive sectors (30–32) of the extended mission in ultra-short-cadence (USC) mode. These observations started on 4 July 2020 and ended on 26 August 2020. From this 84-day data set, we calculated the FT of the USC data up to the Nyquist frequency of 25 000 μHz. In this way, we identified 3 additional combination frequencies that are not detectable in the 120 s cadence data (Fig. 5 bottom). These combination frequencies are given in Table 5. In Fig. 5, we compare the two data sets showing the FT from 120 s-resolution (upper panel) and 20 s-resolution data (lower panel). From the USC data, we extracted three

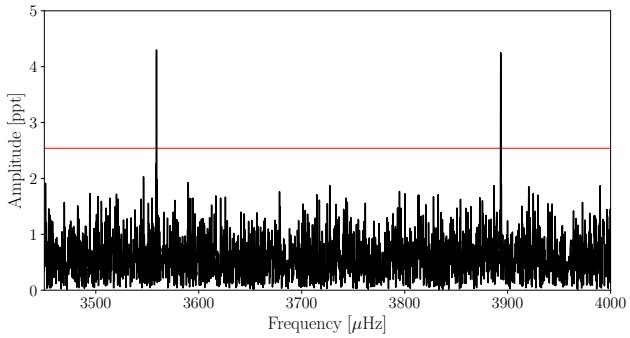

Fig. 4. Main pulsational modes (f_1 and f_2) in EC 20058−5234 presented in Table 4 based on sector 13. The red dashed line denotes the 0.1% FAP.

Table 4. Independent frequencies, periods, and amplitudes (and their uncertainties) and the signal-to-noise ratio in the data of EC 20058.

Peak	ν (μHz)	Π (s)	A (ppt)	S/N
f_1	3558.935(27)	280.983(20)	4.31(53)	6.5
f_2	3893.289(28)	256.852(20)	4.25(53)	6.4

independent periodicities at 2236 μHz (f_1), 2361 μHz (f_3) and 2972 μHz (f_4). 2359 μHz (f_2) and 3861 μHz (f_5) are not detected in USC data. The frequencies at 2359.142 and 2361.678 μHz can be considered as two components of a rotationally split dipole mode. These two peaks are shown in Fig. 6 with frequency splitting of 2.536 μHz. If we assume that the central azimuthal component ($m = 0$) is missing, then the rotation period of EC 04207 would be 2.28 d. On the other hand, if the missing frequency was one of the side components ($m = +1$ or -1), then the rotation period of EC 04207 would be 1.14 d. This solution is consistent with what has been discovered for other types of pulsating WDs, such as GW Vir pulsating stars, which range from 5 h to a few days (Córsico et al. 2019a, 2021; Uzundag et al. 2022) and DAV pulsating stars, which range from 1 h to a 4.2 days (Kawaler 2015; Hermes et al. 2017a).

Combining the results from sectors 4, 5, 30, 31 and 32, we detect five independent frequencies which are concentrated between 2236 μHz and 2972 μHz. We also detect three combination frequencies beyond 4400 μHz. The extracted frequencies are listed in Table 5 with their associated errors and S/N.

3.4. WDJ152738.4-450207.4

WDJ152738.4-450207.4 is a new pulsating DBV star that was observed in sector 12 (2019-May-21 to 2019-Jun-19, cycle 1) and in sector 38 (2021-Apr-28 to 2021-May-26) with 20-s cadence. Within 21 arcsec, the field of view (FOV) includes 21 targets. All these targets are fainter than $G_{\rm mag} = 18$, which is beyond the detection limit of TESS. The crowded field causes enough light contamination to significantly raise the FT noise level, as reported in Table 2. From the short-cadence observations, we detect two significant frequencies near 1341 and 1539 μHz (f_1 and f_5 in Table 6) above the 0.1%FAP level of 20.7 ppt.

The data from sector 38 have a time span of 26.33 d (97.5% duty cycle) including 109476 data points. The frequency resolution is 0.44 μHz. We detect two independent frequencies near 1422 and 1425 μHz. Moreover, we detect a combination frequency at 2845.25 μHz (≃1422 × 2). All the detected frequencies of WD J1527 are reported in Table 6. In Fig. 7 we display the Fourier transform of data taken in sector 12 (upper panel) and sector 38 (lower panel) of WD J1527. The horizontal red line indicates the 0.1% FAP level. In sector 38, a clear triplet pattern can be seen from the sliding FT of the ultra-short-cadence data of WD J1527. We detect a candidate for rotational triplet ($\ell = 1$) at 1419.97 (f_2), 1422.69 (f_3) and 1425.00 μHz (f_4) with a rotational splitting of ∼2.51 μHz. The lower-frequency component at ∼1420 μHz is not present in overall FT, while it is clearly seen in the sFT as shown in Fig. 8. Therefore, even though this side component is below the detection threshold, we include it in our final frequency list with a S/N of 3.5. Multiplets in the frequency spectrum of a pulsating WD are useful both to identify the harmonic degree of the pulsation modes and to measure the rotation period of the star. We show in Fig. 8 the rotational triplet detected

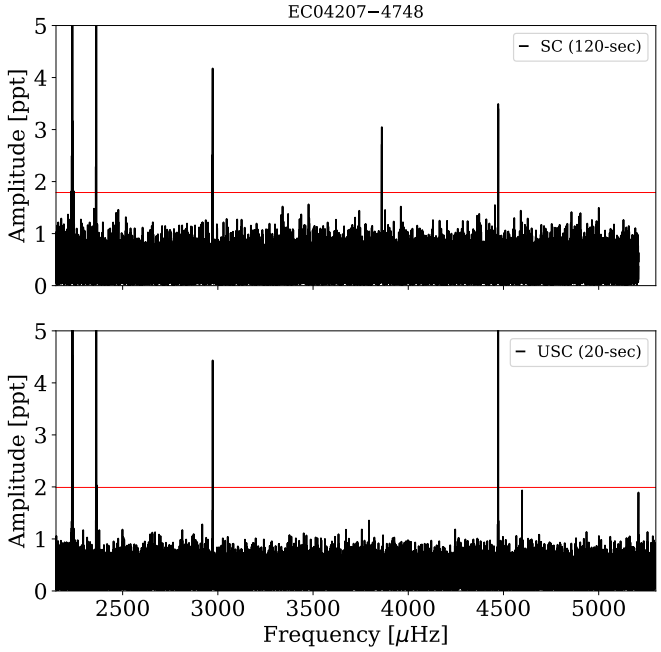

Fig. 5. *Top*: Fourier transform of data taken in sectors 4 and 5 of EC 04207. *Bottom*: Fourier transform of data taken in sectors 30, 31 and 32 of EC 04207. The horizontal red line indicates the 0.1% FAP level.

Table 5. Identified frequencies (combination frequencies), periods, and amplitudes (and their uncertainties) and the signal-to-noise ratio in the data of EC 04207.

Peak	ν (μHz)	Π (s)	A (ppt)	S/N
f_1 (††)	2236.165(00)	447.194(02)	22.87(26)	69.3
f_2	2359.142(18)	423.882(34)	2.14(33)	5.3
f_3 (††)	2361.678(03)	423.427(06)	5.66(26)	17.1
f_4 (††)	2972.672(04)	336.397(05)	4.44(26)	13.4
$2f_1$ (†)	4472.332(03)	223.597(02)	5.18(26)	15.7
$(f_1 + f_3)$ (†)	4597.837(10)	217.493(05)	1.93(26)	5.8
$(f_1 + f_4)$ (†)	5208.833(10)	191.981(04)	1.89(26)	5.7

Notes. The frequencies that are detected only in sectors 4 and 5 are unmarked. Frequency and amplitude from sectors 30–32 are marked with †. Frequency and amplitude that are detected in all sectors marked with ††.

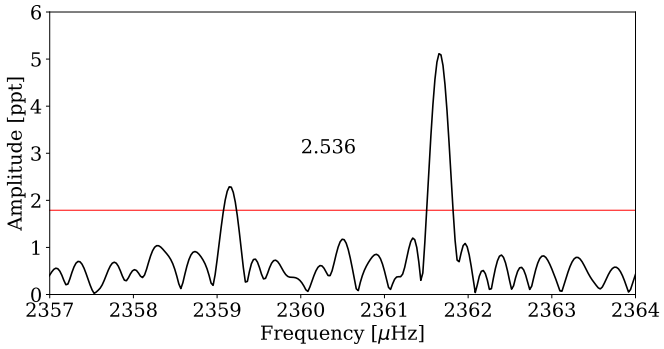

Fig. 6. Close up of the amplitude spectrum of EC 04207 focusing on the potential rotational multiplet with components at 2369 and 2361 μHz.

Table 6. Identified frequencies (combination frequencies), periods, and amplitudes (and their uncertainties) and the signal-to-noise ratio in the data of WD J1527.

Peak	ν (μHz)	Π (s)	A (ppt)	S/N
f_1	1340.703(28)	745.877(15)	30.74(3.89)	7.1
f_2 (†)	1419.967(55)	704.241(27)	6.91(1.61)	3.5
f_3 (†)	1422.687(02)	702.895(01)	17.28(1.61)	8.5
f_4 (†)	1425.000(25)	701.754(12)	15.24(1.61)	7.5
f_5	1539.889(25)	649.397(11)	37.41(3.89)	7.9
$2f_3$	2845.254(42)	351.462(05)	8.94(0.31)	4.6

Notes. The frequencies that are detected only in sector 12 are unmarked. Frequency and amplitude from sector 38 are marked with †.

in WD J1527. The average of the splitting is ∼2.51 μHz, which translates into a rotation period $P_{\rm rot}$ ∼ 2.3 days for WD J1527. Since the frequency spectrum of WD J1527 is admittedly scarce, so that we cannot search for a dipole or quadrupole period spacing using only these three periods extracted from the TESS data.

Finally, we performed time series photometry of WD J1527 with the IxON camera on the 1.6-m Perkin Elmer Telescope at the Pico Dos Dias Observatory during two nights, one in April and one in June 2021. We observed a total of ∼6 h, with integration times from 6 s to 12 s, using a red blocking filter BG40. We reduced the data with the software IRAF, using the task DAOFOT and obtain a light curve using differential photometry. Finally, we obtained the Fourier Transform using the software `PERIOD04` (Lenz & Breger 2005). The list of frequencies, periods and variation amplitudes are listed in Table 7. In Fig. 9 we depict the light curve (top) and the Fourier transform (bottom) for WD J1527 obtained from these ground-based observations. The plotted data are one 4 h run, so there are no gaps to produce aliases. The same peaks are detected when we add the 2 h data from June 21. We note that the ground-based data can detect periods not seen with TESS. This is because the 1.6 m telescope used has an area more than 100 times larger than TESS and therefore can reach fainter magnitudes.

3.5. L 7−44

L 7−44 is also a new pulsating DBV star, which was observed by TESS in short cadence mode during sectors 12 and 13 between 21 May 2019 and 18 July 2019, covering about 57 days. This provides a frequency resolution of 0.14 μHz. The FT average noise level is 0.28 ppt. The 0.1% FAP confidence level is 1.39 ppt.

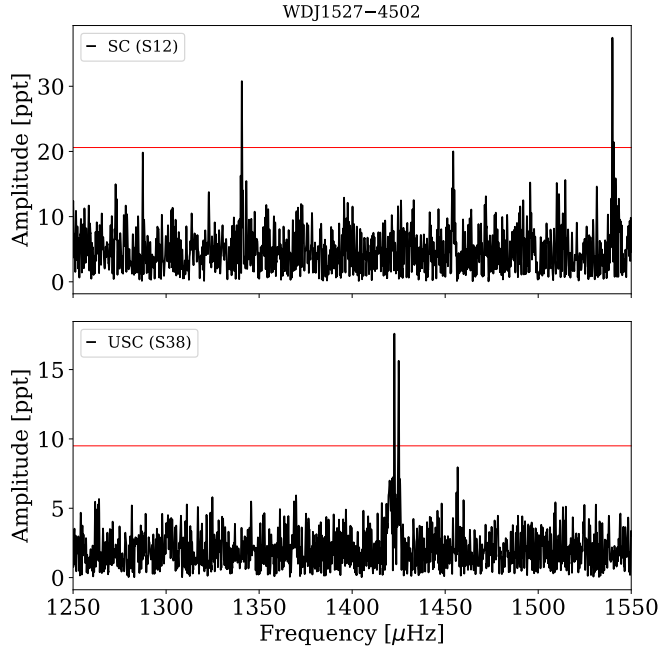

Fig. 7. *Top*: Fourier transform of data taken in sector 12 of WD J1527. The horizontal red line indicates the 0.1% FAP level. *Bottom*: Fourier transform of data taken in sector 38. The horizontal red line indicates the 0.1% FAP level.

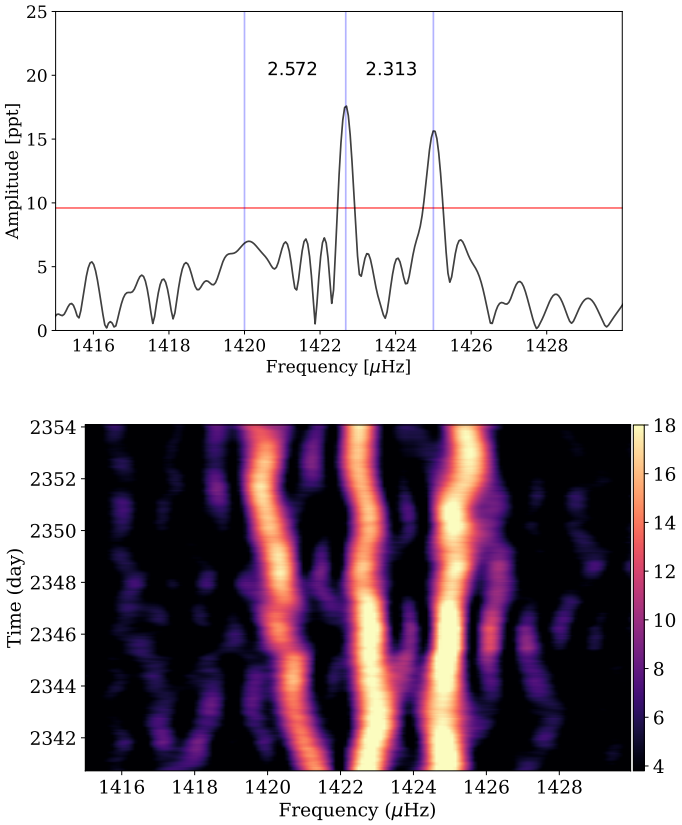

Fig. 8. Detected rotational triplet in WDJ152738.4-450207.4. *Top panel*: Fourier transform of data taken in sector 38. The horizontal red line presents the 0.1% FAP level. We indicated the azimuthal orders (vertical blue lines) of dipole modes and the rotational splitting. *Bottom panel*: Depicts the Sliding Fourier Transform of the same sector covering the same frequency region. The color-scale shows amplitude in ppt units.

Table 7. Detected periods for WDJ152738.4−450207.4 from ground-based observations performed at the Pico do Dias observatory.

Peak	ν (μHz)	Π (s)	A (ppt)	S/N
f_1	1425.7(67)	701.89(33)	24.16	18.6
f_2	2290.6(67)	436.98(13)	5.71	4.4
f_3	2831.2(67)	352.93(8)	5.60	4.3
f_4	4283.9(67)	233.26(4)	4.69	3.6

Notes. Column 2 corresponds to the frequencies, Col. 3 shows the periods, and Col. 4 the amplitudes. Finally, Col. 5 gives the S/N level for each mode.

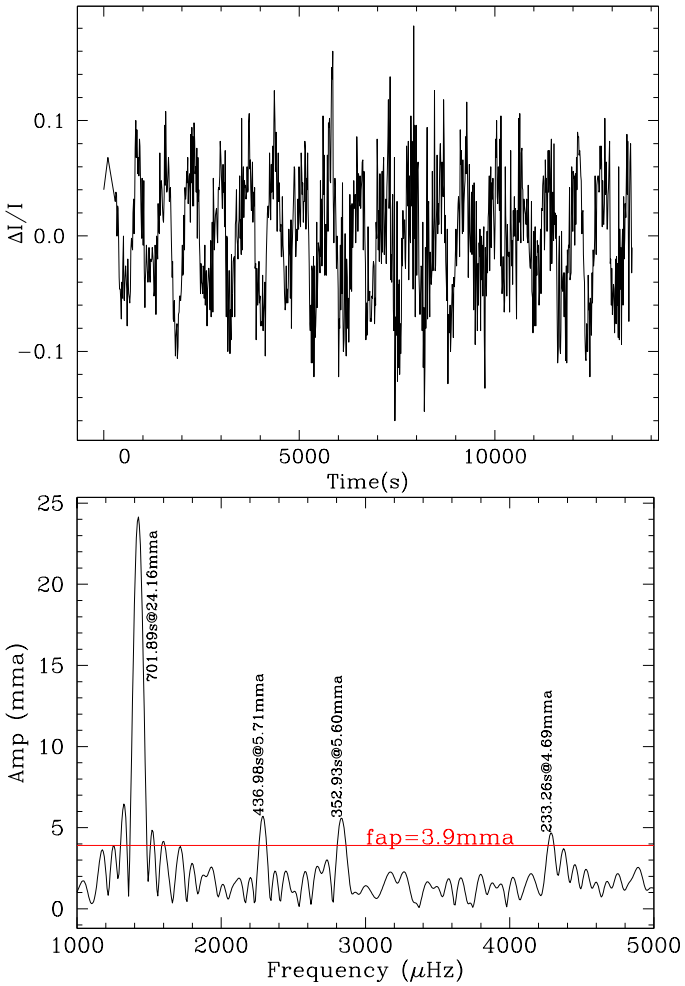

Fig. 9. *Upper panel*: Light curve of the ground-based observations of WD J1527 carried out with Perkin Elmer Telescope. The plotted data is one 4 h run. *Lower panel*: Fourier transform, with a false-alarm pobability FAP(1/1000) = 3.9 mma.

We detect four frequencies at 981.22 (f_1), 1067.52 (f_2), 1094.50 (f_5) and 2141.81 μHz (f_6).

L 7−44 was also observed in sector 39 in 20-s cadence during 27 d. The frequency resolution of this dataset is 0.41 μHz. We identified four frequencies above 0.1% FAP confidence level of 1.84 ppt, which are listed in Table 8. We found a complicated pattern around 1092 μHz, that is depicted in Fig. 10. This unresolved structure is most likely due to frequency and/or phase variations over the length of the data. Also, it could be caused by mode incoherence, that is, since this is the lowest frequency pulsation mode in this sample, it could be incoherent because it is reflecting off the moving base of the outer convection zone, as described for DAVs in Montgomery et al. (2020). We extracted three frequencies (f_2, f_3 and f_4) from this region. However, only f_3 will be used for the asteroseismic modeling of this star since it is the highest FT peak.

Table 8. Independent frequencies, periods, and amplitudes (and their uncertainties) and the signal-to-noise ratio in the data of L 7−44.

Peak	ν (μHz)	Π (s)	A (ppt)	S/N
f_1	981.221(21)	1019.138(21)	1.64(31)	4.6
f_2	1067.521(19)	936.750(17)	1.80(31)	4.7
f_3 (†)	1091.211(28)	916.413(23)	2.49(30)	7.1
f_4 (†)	1093.003(27)	914.910(23)	2.53(30)	7.2
f_5 (††)	1094.528(35)	913.636(29)	1.96(30)	5.6
f_6 (††)	2141.813(16)	466.894(4)	2.09(31)	5.5

Notes. Frequency and amplitude from both short and ultra-short cadence data are marked with ††. Frequency and amplitude from sector ultra-short cadence data are marked with †. The frequencies that are detected only in sector short-cadence data are unmarked.

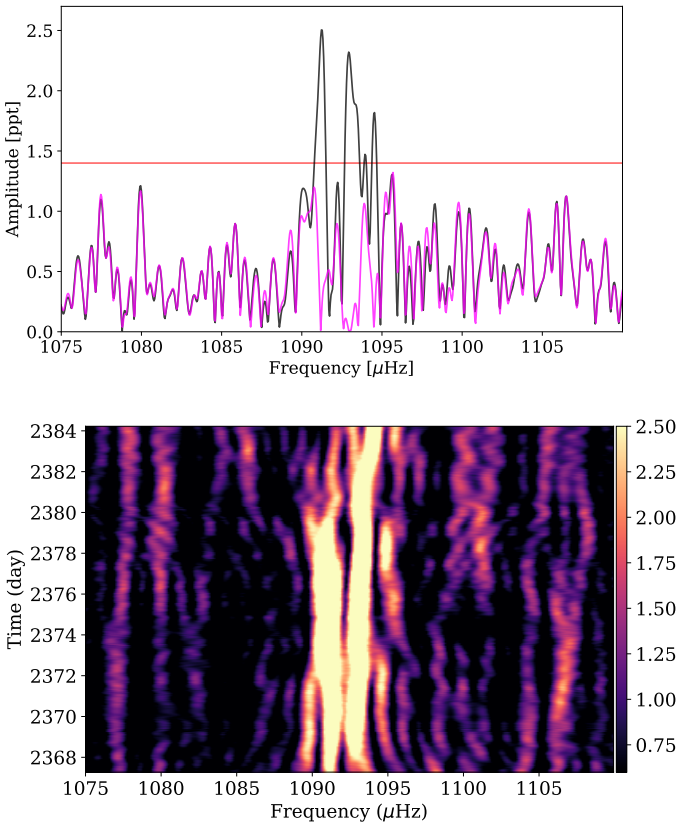

Fig. 10. *Top*: Fourier transform of sector 39 data of L 7−44. The horizontal red line indicates the 0.1% FAP level. The magenta line is the residual after extraction of the signals. *Bottom*: Sliding Fourier transform of sector 39 data of L 7−44. The color-scale illustrates amplitude in ppt units.

4. Evolutionary models and spectroscopic masses

We employ a set of state-of-the-art DB WD stellar models that take into account the complete evolution of the progenitor

stars, assuming that DB WDs are descendants of the PG 1159 stars after going through the DO WD stage. The models were extracted from the evolutionary calculations of Althaus et al. (2009) produced with the LPCODE evolutionary code (see that paper for details). These DB WD models have been employed in the asteroseismic analyses of the DBV stars KIC 8626021 (Córsico et al. 2012), KUV 05134+2605 (Bognár et al. 2014), PG 1351+489 (Córsico et al. 2014), WD 0158−160 (Bell et al. 2019), and GD 358 (Córsico et al. 2022). The sequences of DB WD models have been obtained taking into account a complete treatment of the evolutionary history of progenitors stars, starting from the zero-age main sequence (ZAMS), through the thermally pulsing asymptotic giant branch (TP-AGB) and born-again (VLTP; very late thermal pulse) phases to the domain of the PG 1159 stars, and finally the DB WD stage. As such, they are characterized by evolving chemical profiles consistent with the prior evolution. We varied the stellar mass and the effective temperature in our model calculations, while the He content, the chemical structure at the CO core, and the thickness of the chemical interfaces were fixed by the evolutionary history of progenitor objects. The models employ the ML2 prescription of convection with the mixing length parameter, α, fixed to 1 (Bohm & Cassinelli 1971; Tassoul et al. 1990). Specifically, we considered nine DB WD sequences with stellar masses of: 0.515, 0.530, 0.542, 0.565, 0.584, 0.609, 0.664, 0.741, and $0.870 M_{\odot}$. These DB WD sequences are characterized by the maximum He-rich envelope that can be left by prior evolution if we assume that they are the result of a born-again episode. The value of envelope mass ranges from $M_{\rm He}/M_{*} \sim 2 \times 10^{-2}$ ($M_{*} = 0.515\, M_{\odot}$) to $M_{\rm He}/M_{*} \sim 1 \times 10^{-3}$ ($M_{*} = 0.870\, M_{\odot}$). In Fig. 1 we show the complete set of DB WD evolutionary tracks (with different colors according to the value of the stellar mass) along with the location of all the DBVs known to date (Córsico et al. 2019a; Duan et al. 2021; Vanderbosch et al. 2022) and the two new DBVs reported in this paper for the first time.

We computed $\ell = 1, 2$ g-mode pulsation periods in the range 80–1500 s with the adiabatic and nonadiabatic versions of the pulsation code LP-PUL (Córsico & Althaus 2006; Córsico et al. 2006) and the same methods we employed in the previous works of La Plata Stellar Evolution and Pulsation Research Group[2]. Employing the evolutionary tracks presented in Fig. 1 and the values of the spectroscopic surface gravity and temperature shown in Table 1, we derive a value of the spectroscopic mass of each of the five analyzed stars by interpolation. It is worth noting that we use the same set of DB WD models both for estimate the spectroscopic mass and also to assess the stellar mass from the period spacing (next Section). For PG 1351 we obtain $M_{\star} = 0.558 \pm 0.027\, M_{\odot}$. In the case of EC 20058 and EC 04207, we derive $M_{\star} = 0.614 \pm 0.030\, M_{\odot}$ and $M_{\star} = 0.515 \pm 0.023\, M_{\odot}$, respectively. Finally, we obtain $M_{\star} = 0.675 \pm 0.022\, M_{\odot}$ for WD J1527, and $M_{\star} = 0.630 \pm 0.016\, M_{\odot}$ for L 7−44. The uncertainties in the stellar mass are estimated from the uncertainties in $T_{\rm eff}$ and $\log g$ by adopting the extreme values of each parameter when interpolating between the evolutionary tracks of Fig. 1.

5. Asteroseismological analysis

The asteroseismological methods we use in this paper to extract information of the stellar mass and the internal structure of the DBV stars PG 1351, EC 20058, EC 04207, WD J1527, and L 7−44 are the same used in, for instance, Córsico et al. (2022) for the DBV star GD 358 observed with TESS.

First, we attempt to infer the stellar mass, when possible, by comparing the observed mean period spacing, $\Delta\Pi$, with the average of the computed period spacings ($\overline{\Delta\Pi_k}$). The mean period spacing is assessed through the Kolmogorov-Smirnov ($K-S$; Kawaler 1988), and the inverse variance ($I-V$; O'Donoghue 1994) significance tests. On the other hand, the average of the computed period spacings is calculated as $\overline{\Delta\Pi_k} = (N-1)^{-1} \sum_k \Delta\Pi_k$, where the "forward" period spacing ($\Delta\Pi_k$) is defined as $\Delta\Pi_k = \Pi_{k+1} - \Pi_k$ (k being the radial order) and N is the number of computed periods laying in the range of the observed periods. The present method relies on the spectroscopic effective temperature, so the results are unavoidably affected by its associated uncertainty. This method takes full advantage of the fact that the period spacing of DBV stars primarily depends on the stellar mass and the effective temperature, and very weakly on the thickness of the He envelope (see, e.g., Tassoul et al. 1990).

Another asteroseismological tool to disentangle the internal structure of DBV stars is to seek theoretical models that best match the individual pulsation periods of the target star. To measure the goodness of the match between the theoretical pulsation periods ($\Pi_{\ell,k}$) and the observed individual periods ($\Pi_i^{\rm o}$), we compute the quality function $\chi^2(M_{\star}, T_{\rm eff}) = \frac{1}{N} \sum_{i=1}^{N} \min[(\Pi_{\ell,k} - \Pi_i^{\rm o})^2]$, where N is the number of observed periods. In order to find the stellar model that best fits the observed periods exhibited by each target star – the "asteroseismological" model –, we evaluate the function χ^2 for stellar masses $0.515 \leq M_{\star}/M_{\odot} \leq 0.870$. For the effective temperature, we employ a much finer grid ($\Delta T_{\rm eff} = 10 - 30$ K). For each target star, the DB WD model that shows the lowest value of χ^2 is adopted as the best-fit asteroseismological model. To quantitatively assess the quality of our period fit, we compute the average of the absolute period differences, $\overline{\delta\Pi_i} = \left(\sum_{i=1}^{N} |\delta\Pi_i|\right)/N$, where $\delta\Pi_i = (\Pi_{\ell,k} - \Pi_i^{\rm o})$, and the root-mean-square residual, $\sigma = \sqrt{(\sum_{i=1}^{N} |\delta\Pi_i|^2)/N} = \sqrt{\chi^2}$. To have a global indicator of the goodness of the period fit that takes into account the number of free parameters, the number of fitted periods, and the proximity between the theoretical and observed periods, we compute the Bayes Information Criterion (BIC; Koen & Laney 2000), defined as $\mathrm{BIC} = n_{\rm p} \left(\frac{\log N}{N}\right) + \log \sigma^2$, where $n_{\rm p}$ is the number of free parameters of the stellar models, and N is the number of observed periods, that is, the number of periods that we want to match. The smaller the value of BIC, the better the quality of the fit. In our case, $n_{\rm p} = 2$ (stellar mass and effective temperature). It is important to note that this criterion penalizes for an excess of parameters ($n_{\rm p}$). Below, we employ the tools described above to extract information from the DBV stars considered in this work.

5.1. PG 1351+489

For this star, TESS detects a single period of 489.26 s which is likely associated with an eigenmode of the star (see Table 3). The other period present (~244.630 s) corresponds to twice the frequency of that single period. The period of ~489 s is present also in the data acquired through the ground-based monitoring by Redaelli et al. (2011), who identified four independent periods (see their Table 2). In Fig. 11 we schematically show the period spectrum detected with TESS (upper panel), and the periods detected by Redaelli et al. (2011; lower panel), with amplitudes set to unity to facilitate visualization. Unfortunately, the TESS data do not broaden the period spectrum of PG 1351 in

[2] http://fcaglp.fcaglp.unlp.edu.ar/evolgroup/

Table 9. Periods of PG 1351 available for the asteroseismological analysis.

$\Pi_i^{\rm O}$ (s) REA11	$\Pi_i^{\rm O}$ (s) TESS	$\Pi_{\ell,k}$ (s)	ℓ	k	$\delta\Pi_{\ell,k}$ (s)	$\dot{\Pi}_{\ell,k}$ (10^{-13}) s/s	Unstable
335.26		336.81	2	13	−1.55	0.60	Yes
489.33	489.26	489.47	1	11	−0.21	0.81	Yes
584.68		586.99	2	25	−2.31	1.02	Yes
639.63		639.37	1	15	0.26	1.19	Yes

Notes. Column 1 corresponds to four $\ell = 1$ periods measured by Redaelli et al. (2011; REA11), and Col. 2 corresponds to the single period detected by TESS (Table 3). The third, fourth and fifth columns give the theoretical periods of the asteroseismological model of PG 1351, the harmonic degree and the radial order, respectively. Columns 6 and 7 correspond to the period difference ($\delta\Pi_k = \Pi_i^{\rm O} - \Pi_k$) and the rate of period change, respectively. Finally, the last column provides information about the pulsational stability or instability nature of the modes.

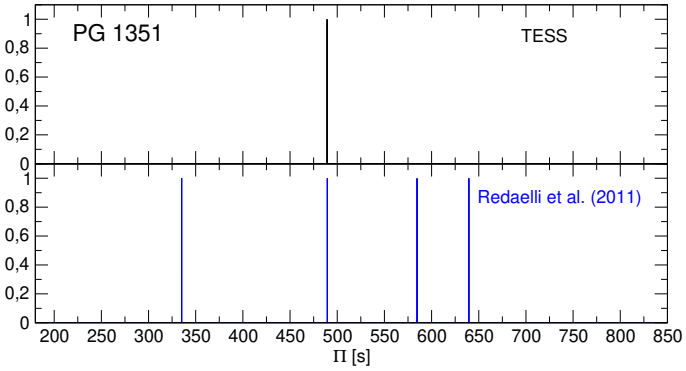

Fig. 11. Schematic distribution of the pulsation periods of PG 1351 according to TESS (6 periods, black lines, *upper panel*), and according to Redaelli et al. (2011; 4 periods, blue lines, *lower panel*). The amplitudes have been arbitrarily set to one for clarity.

relation to the periods already known with observations from the ground. The list of periods of the star is shown in Table 9. With this very limited list of periods, we have tried to find a possible mean period spacing to infer some hint of the stellar mass of PG 1351.

In Fig. 12 we show the results of applying the $I-V$ and $K-S$ statistical tests to the set of four periods of Table 9. We are aware that with only four periods, it is feasible to find different period spacing values that fit the distribution of those periods. Indeed, the two tests show hints of several possible constant period spacings of ∼11 s, ∼14 s, ∼19 s, ∼25 s, ∼31 s, and another at ∼50 s. Since the period spacing in DB WDs depends mainly on the stellar mass and the effective temperature, we can explore which of these possible period spacings are compatible with the range of stellar masses of DB WDs. We have computed the average of the theoretical period spacings for $\ell = 1$ and $\ell = 2$, $\overline{\Delta\Pi_k}$, in terms of the effective temperature for all the masses considered and a period interval of 300−650 s. In Fig. 13 we show $\overline{\Delta\Pi_k}$ with curves of different colors to distinguish the different stellar masses, corresponding to $\ell = 1$ (upper panel) and $\ell = 2$ (lower panel) modes. We note that the only period spacings compatible with reasonable stellar masses are ∼31 s for $\ell = 1$ and ∼19 s for $\ell = 2$. Both possible period spacings point to a stellar mass somewhat high for DB WD standards, but still possible, in the

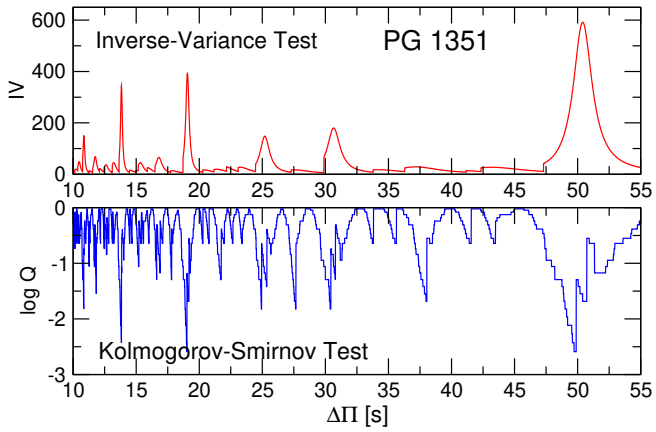

Fig. 12. $I-V$ (*upper panel*) and $K-S$ (*lower panel*) significance tests to search for a constant period spacing in PG 1351. The tests are applied to the set of 4 pulsation periods of Table 9, that includes the TESS and Redaelli et al. (2011)'s periods. Several possible constant period spacings are evident, the most notorious being that of ∼50 s. See text for details.

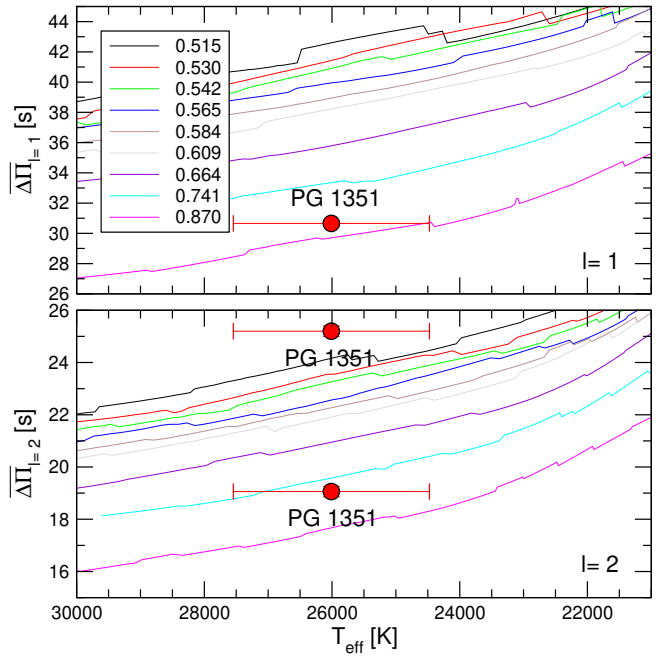

Fig. 13. Dipole (*upper panel*) and quadrupole (*lower panel*) average of the computed period spacings, $\overline{\Delta\Pi_k}$, assessed in a range of periods that includes the periods observed in PG 1351, shown as curves of different colors according to the different stellar masses. We consider the effective temperature $T_{\rm eff} = 26\,010 \pm 1536$ K (Bergeron et al. 2011), and the possible period spacing values derived from the four periods of PG 1351 according to Table 9. We include the error bars associated with the uncertainties in $\overline{\Delta\Pi_k}$ and $T_{\rm eff}$.

range 0.74−0.87 $M_\odot$[3]. However, we emphasize that, since the number of available periods is very low, the derivation of the

[3] We note that there is also a possible period spacing of ∼25 s. If this were a $\ell = 1$ period spacing, the mass of PG 1351 should be very high (∼1$M_\odot$). Alternatively, if this were a $\ell = 2$ period spacing, then the mass of PG 1351 should be too low (∼0.40$M_\odot$). Both cases have to be discarded because they are in serious conflict with the spectroscopic determination of $\log g$, that indicates a stellar mass in the range $0.53 \lesssim M_\star/M_\odot \lesssim 0.59$ (see Fig. 1).

Table 10. Main characteristics of the DBV star PG 1351.

Quantity	Spectroscopy Astrometry	Asteroseismology
$T_{\rm eff}$ [K]	26 010 ± 1536	25 775 ± 150
$M_\star$ [$M_\odot$]	0.558 ± 0.027	0.664 ± 0.013
$\log g$ [cm/s^2]	7.91 ± 0.07	8.103 ± 0.020
$\log(L_\star/L_\odot)$		−1.244 ± 0.03
$\log(R_\star/R_\odot)$		1.912 ± 0.015
$(X_{\rm C}, X_{\rm O})_{\rm c}$		0.32, 0.65
$M_{\rm He}/M_\star$		5.42×10^{-3}
d [pc]	$175.73^{+1.53(a)}_{-1.58}$	$167.05^{+2.31}_{-2.26}$
π [mas]	$5.69 \pm 0.05^{(a)}$	$5.99^{+0.08}_{-0.09}$

References. (a) *Gaia* EDR3.

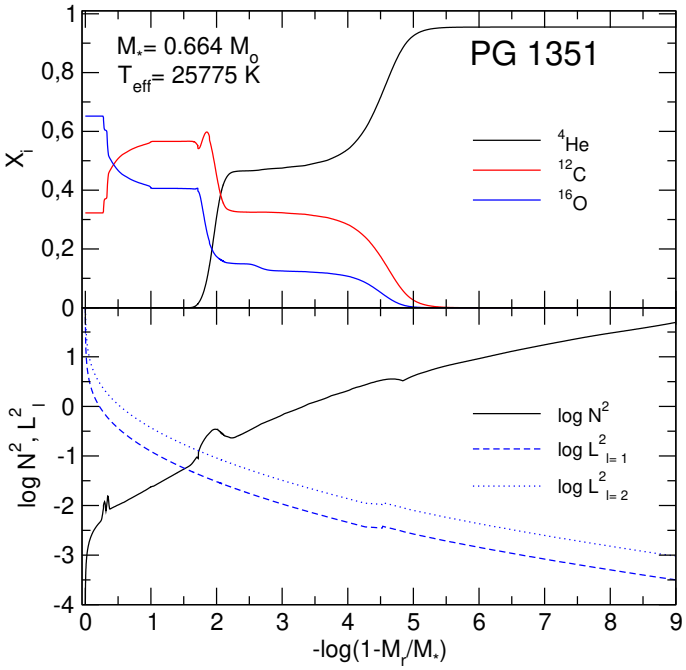

Fig. 14. Chemical profiles (*upper panel*) and the squared Brunt-Väisälä and Lamb frequencies for $\ell = 1$ and $\ell = 2$ (*lower panel*) corresponding to our asteroseismological DB WD model of PG 1351 with a stellar mass $M_\star = 0.664\,M_\odot$ and an effective temperature $T_{\rm eff} = 25\,775$ K.

period spacing is not robust, and the stellar mass by this mean is not significantly constrained.

A detailed asteroseismological analysis of PG 1351 employing the same DB WD models considered in this paper was already carried out by Córsico et al. (2014). The only difference is that in that work, the authors used a period of 489.33 s, instead of 489.26 s as in the present paper (see Table 3). Since this difference is completely negligible to the limit of our investigation, the asteroseismological model that we obtain in this work is the same as in Córsico et al. (2014) and we do not repeat that analysis here. We show in Table 9 the theoretical periods and the harmonic degree and radial order of this model, along with the period differences and the rates of period change. We obtain $\overline{\delta\Pi_i} = 1.08$ s, $\sigma = 1.40$ s, and BIC = 0.59 for the asteroseismological model. We note that Córsico et al. (2022) obtain BIC = 1.13 for the asteroseismological model of GD 358 and Bischoff-Kim et al. (2019) obtain BIC = 1.2 for their best period fit to the same star. So, the low value of BIC obtained in this work for PG 1351 indicates that our period fit is very good. We show the characteristics of this model ($M_\star = 0.664\,M_\odot$, $T_{\rm eff} = 25\,775$ K) in Table 10[4], and we plot its internal chemical profiles (upper panel) and the logarithm of the squared Brunt-Väisälä and Lamb frequencies (lower panel) in Fig. 14.

Córsico et al. (2014) show that there are other possible asteroseismological solutions, as can be seen in their Fig. 9 and Table 1. We note (as those authors do) that the possible solution that assumes only $\ell = 1$ modes has a very low quality of the period fit, and can be discarded. The two solutions with $M_\star = 0.87\,M_\odot$ and assuming a mix of $\ell = 1$ and $\ell = 2$ modes can be discarded too, in one case due to poor quality of the period fit, and in the other one because the $T_{\rm eff}$ is too low. As an additional argument to discard these three possible solutions, we emphasize the fact that they correspond to a stellar mass ($M_\star = 0.87\,M_\odot$), which is too large compared to the spectroscopic one ($M_\star = 0.56\,M_\odot$) and in severe contradiction with the surface gravity derived for this star. Finally, none of these three possible solutions fit *Gaia's* distance better than the asteroseismological model of Table 10 (see below).

We have examined the pulsational stability and instability nature of the modes associated with the periods fitted to the observed ones. We adopted the frozen-in convection approximation (Unno et al. 1989). In particular, we examined the sign and magnitude of the linear nonadiabatic growth rates, $\eta_k = -\Im(\sigma_k)/\Re(\sigma_k)$, where $\Re(\sigma_k)$ and $\Im(\sigma_k)$ are the real and the imaginary parts, respectively, of the complex eigenfrequency σ_k. We find that the periods of the asteroseismological model of PG 1351 are associated with unstable modes, in line with the observational evidence. A common fact in all nonadiabatic calculations of pulsations in WDs, but also in any other class of pulsating stars, is that in general the models predict many more unstable modes than are observed. PG 1351 is no exception. There must be some (unknown) filter mechanism that selects some unstable modes and gives them large, observable amplitudes, while the other unstable modes never reach those amplitudes and are not observed.

Finally, using the asteroseismological model of PG 1351, we can assess the seismic distance of the star. We employed the effective temperature and gravity of our best-fit model to infer the absolute G magnitude (M_G) in the *Gaia* photometry. This was done by computing a DB WD atmosphere model using $T_{\rm eff}$ and $\log g$ of the asteroseismological model. We find $M_G = 10.564$ mag. With the observed *Gaia* magnitude, $m_G = 16.678$ mag, a distance modulus was calculated as $m_G - M_G$, and this was converted to a seismological distance d using $\log(d_{\rm s}) = (m_G - M_G + 5)/5$. We obtained $d_{\rm s} = 167.05^{+2.31}_{-2.26}$ pc, where the errors were calculated from the errors of $T_{\rm eff}$, $\log g$, and m_G. The atmosphere models used $\log({\rm H/He}) = -5$. A test calculation showed that the difference to pure He models is negligible. The seismological distance is in agreement with the value derived by Bergeron et al. (2011; ∼166 pc), and is just ∼5% lower than the astrometric distance measured by *Gaia* EDR3, of $175.73^{+1.53}_{-1.58}$ pc. Finally, because TESS has detected a single eigenfrequency in PG 1351 ($\nu \sim 2044$ μHz), we have not been able to confirm (or discard) the rotation period of 8.9 h derived by Redaelli et al. (2011).

[4] Here, $M_{\rm He}/M_\star$ is the total mass content of He in units of the stellar mass.

Table 11. Enlarged list of periods of EC 20058.

$\Pi_i^{\rm O}$ (s) SEA08	$\Pi_i^{\rm O}$ (s) TESS	$\Pi_{\rm fit}^{\ell=1}$ (s)	$\delta\Pi^{\ell=1}$ (s)	$\Pi_{\rm fit}^{\ell=2}$ (s)	$\delta\Pi^{\ell=2}$ (s)	$\ell^{\rm O}$
195.0(*)		193.662	1.338			1
204.6						?
207.6(**)				208.572	−0.972	2
256.9	256.852(**)			256.162	0.69	2
274.7(*)		276.485	−1.785			1
281.0	280.983(**)			279.957	1.026	2
286.6						?
333.5						?
350.6(**)				351.342	−0.742	2
525.4(*)		524.954	0.446			1
539.8						?

Notes. Column 1 corresponds to 11 $\ell = 1$ periods derived by Sullivan et al. (2008; SEA08; see also Table 1 of Bischo-Kim & Metcalfe 2011), and Col. 2 corresponds to two periods detected by TESS (Table 4). The periods with one (two) asterisk(s) are used in a linear least square fit for modes with $\ell = 1$ ($\ell = 2$).

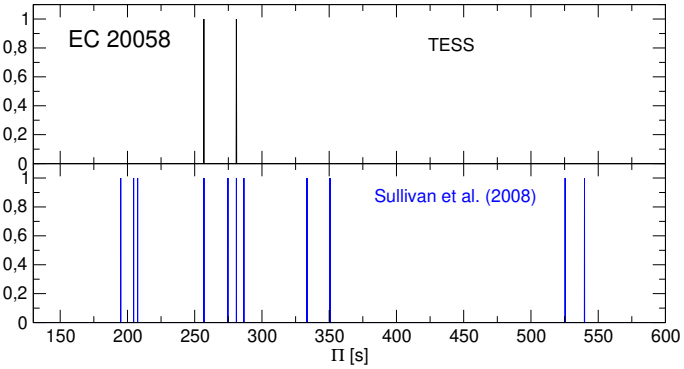

Fig. 15. Schematic distribution of the pulsation periods of EC 20058 according to TESS (2 periods, black lines, *upper panel*), and according to Sullivan et al. (2008; 11 periods, blue lines, *lower panel*). The amplitudes have been arbitrarily set to one for clarity.

5.2. EC 20058−5234

Similar to the case of PG 1351, the pulsation spectrum of EC 20058 detected by TESS is not rich. Indeed, TESS detected only two large-amplitude periods, compared to a total of 11 periods measured with observations from the ground by Sullivan et al. (2008; see Table 11). In Fig. 15 we schematically show the two periods detected with TESS (upper panel), and the periods detected by Sullivan et al. (2008; lower panel). For our analysis, in the case of the two periods that are common to both sets, we adopt those detected by TESS, as they are more accurate.

In Fig. 16 we display the results of applying the statistical tests to the set of 11 periods of the first column of Table 11. The tests show hints of several possible constant period spacings, $\Delta\Pi = 12.78, 15.84, 23.90, 26.36, 41.11, 47.67$ s (emphasized with vertical arrows in the figure), suggesting that no simple pattern of period spacing is apparent in the EC 20058 spectrum, in line with previous works (Sullivan et al. 2008). Figure 17 depicts $\overline{\Delta\Pi_k}$ (computed considering a period interval of 200−600 s) with curves of different colors to distinguish the different stellar masses, corresponding to $\ell = 1$ (upper panel) and $\ell = 2$ (lower panel) modes. Based on this figure, the possible extreme values

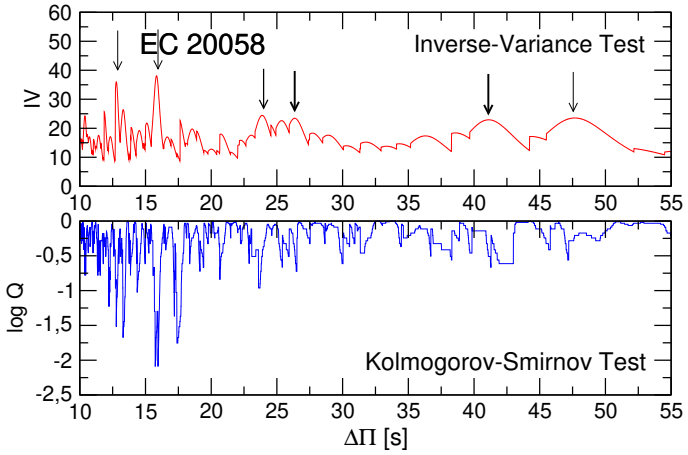

Fig. 16. $I-V$ (*upper panel*) and $K-S$ (*lower panel*) significance tests to search for a constant period spacing in EC 20058. The tests are applied to the set of 11 pulsation periods of Table 11, that includes the TESS plus Sullivan et al. (2008)'s periods. Possible values of constant period spacing are marked with arrows in the *upper panel*.

for constant period spacings, that is 12.78 s and 47.67 s, can be discarded from the analysis because they imply a mass too high or extremely low, respectively. The remaining four values could actually be constant period spacings, and they are plotted in Fig. 17 with red circles. Concentrating on the upper panel (dipole modes), we see that a possible spacing of periods of 41.11 s would indicate a stellar mass of ∼0.55 $M_\odot$ if it corresponds to modes with $\ell = 1$. Regarding the lower panel ($\ell = 2$), we can discard the possible period spacing of ∼26 s because it would indicate a very low mass for EC 20058 ($\lesssim$0.4 $M_\odot$). The possible solutions that remain indicate a stellar mass of ∼0.530 $M_\odot$ if $\Delta\Pi = 23.90$ s, or a stellar mass ∼0.95 $M_\odot$ if $\Delta\Pi = 15.84$ s. We note that a stellar mass as high as ∼0.95 $M_\odot$ is not compatible with the spectroscopic mass of this star, ∼0.61 $M_\odot$. On the other hand, such massive DB WDs are very unusual. For these reasons, we discard the possible solution of ∼16 s for the period spacing. Then, we are left with the possible period spacing of 23.90 s and $\ell = 2$.

In summary, the two most probable period spacings present in the star are $\Delta\Pi_{\ell=1} = 41.11$ s and $\Delta\Pi_{\ell=2} = 23.90$ s. We immediately note that $41.11/23.90 = 1.72$, which is very close to the asymptotic prediction, $\Delta\Pi_{\ell=1}/\Delta\Pi_{\ell=2} = \sqrt{3} \sim 1.732$ (Tassoul et al. 1990). While it is appealing to conclude that the pulsational spectrum of EC 20058 is composed of two patterns of periods, one with $\ell = 1$ and the other with $\ell = 2$, it is not trivial to explain why both patterns suggest different stellar masses (∼0.53 and ∼0.55 $M_\odot$). However, this small discrepancy could be alleviated if more realistic uncertainties in the effective temperature were adopted. Beyond this, the fact that the ratio of the period spacings is so close to that predicted by the asymptotic theory is quite encouraging, and prompts us to try to identify the harmonic degree of each period of EC 20058. To determine the precise period spacings, we performed linear least-squares fits (plotted in the upper panel of Fig. 18) using three periods for the case of $\ell = 1$, and four periods for the case of $\ell = 2$, marked with a single asterisk and two asterisks, respectively, in Table 11. We obtain a dipole period spacing $\Delta\Pi_{\ell=1} = 41.41 \pm 0.39$ s and a quadrupole period spacing $\Delta\Pi_{\ell=2} = 23.80 \pm 0.28$ s. We have four remaining periods (204.6 s, 286.6 s, 333.5 s, and 539.8 s) that do not fit in any of the two period spacing patterns found. They could have harmonic degree $\ell = 1$ and/or $\ell = 2$ and the reason

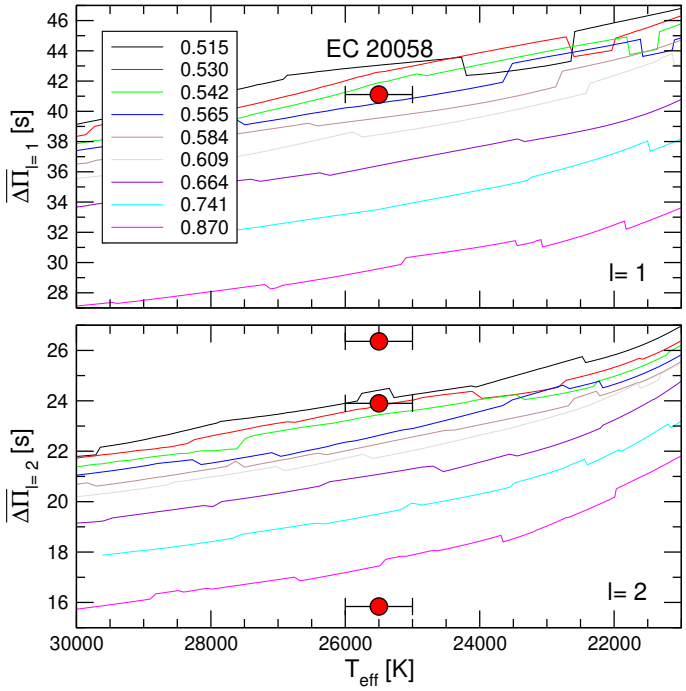

Fig. 17. Dipole ($\ell = 1$, *upper panel*) and quadrupole ($\ell = 2$, *lower panel*) average of the computed period spacings, $\overline{\Delta\Pi_k}$, assessed in a range of periods that includes the periods observed in EC 20058, shown as curves of different colors according to the different stellar masses. We consider the effective temperature $T_{\rm eff} = 25\,500 \pm 500$ K (Koester et al. 2014), and the possible period spacing values $\Delta\Pi = 12.78, 15.84, 23.90, 26.36, 41.11, 47.67$ s (see Fig. 16). For a discussion, see the text.

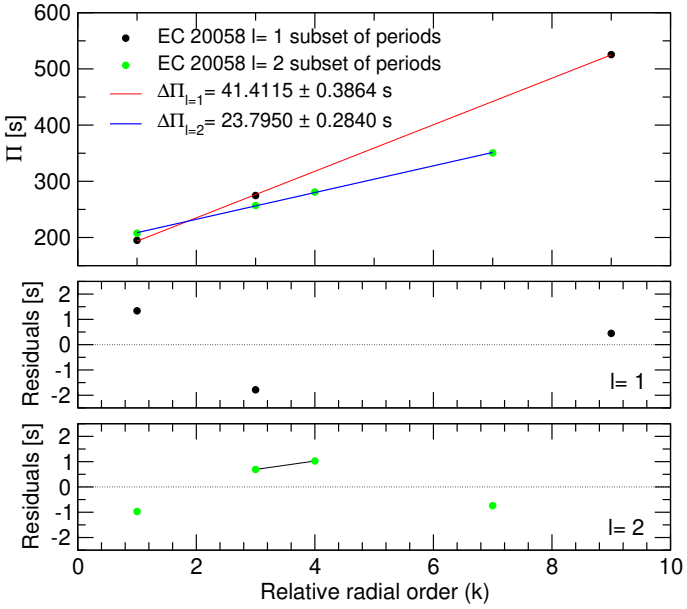

Fig. 18. *Upper panel*: Linear least-squares fits to the three dipole periods of EC 20058 marked with an asterisk and the four quadrupole periods marked with two asterisks in Table 11. The derived period spacings from these fits are $\Delta\Pi_{\ell=1} = 41.4115 \pm 0.3864$ s and $\Delta\Pi_{\ell=1} = 23.795 \pm 0.284$ s, respectively. *Middle panel*: Residuals of the $\ell = 1$ period distribution relative to the dipole mean period spacing. *Lower panel*: Residuals of the $\ell = 2$ period distribution relative to the quadrupole mean period spacing. Modes with consecutive radial order are connected with a thin black line.

for their deviation from the spacings derived for both $\ell = 1$ and $\ell = 2$ modes could be that they are affected by mode trapping (see, e.g., Bradley et al. 1993).

We investigated how the results of the K-S test change with variations in the input frequency list, that is, excluding different periods, one at a time, and ran the test again. We have found that the ∼24 s period spacing is very robust, since, in general, the corresponding minimum in the K-S test becomes steeper or stays the same when one ignores each period. On the other hand, the ∼41 s period spacing is much more sensitive to the specific list of periods on which the test is computed.

A completely different assumption than the one described above is that the period spectrum of EC 20058 has a combination of $\ell = 1$ and $\ell = 2$ modes, but with the possible presence of rotational frequency multiplets. It has been the hypothesis favored by Sullivan et al. (2008; see their Fig. 8). In this scenario, the frequency 4816.8 μHz (period 207.6 s) could be one component of a rotational triplet centered at 4887.8 μHz (204.6 s), the other component being inhibited by an unknown mechanism, and the frequencies 3640.1 μHz (274.7 s) and 3489.0 μHz (286.6 s) could be the two nonzero m components of a rotational triplet centered at 3558.935 μHz (280.983 s). Implicitly, the periods 204.6 s and 280.983 are assumed here to be $\ell = 1$. Using a mean frequency splitting of ∼70 μHz and the asymmetry observed in the frequency splitting of the triplet centered at the frequency 3558.935 μHz, Sullivan et al. (2008) derived a rotation period of ∼2 h and a magnetic field of ∼3 kG for EC 20058. Under the present hypothesis, it is interesting to look for a constant period spacing with the statistical tests, this time neglecting the periods 207.6 s, 274.7 s, and 286.6 s. Our exercise does not indicate any clear constant period spacing in this reduced set of periods. The nonexistence of a constant period spacing could be explained by the fact that some of the periods exhibited by the star are not in the asymptotic regime.

Putting it all together, we face two possible scenarios for EC 20058. According to one of them, we are seeing a combination of ($m = 0$) $\ell = 1$ and $\ell = 2$ excited modes, that conform two patterns of constant period spacing. In this scenario, no frequency multiplets due to rotation are present. In this case, the assignment of the ℓ value for some of the periods is that of Table 11 (Col. 7). In addition, following Sullivan et al. (2008), we can assume the existence of rotational triplets, in this way identifying the periods 204.6 s and 280.983 s with $m = 0$ $\ell = 1$ modes. We cannot rule out or accept conclusively either of these two scenarios. Thus, when performing the period-to-period fits (see below), we have to consider both possibilities for the identification of the harmonic degree of the modes.

In the second part of our analysis of EC 20058, we have performed period fits considering two sets of periods and identifications. One of them corresponds to that indicated in Table 12 (case 1), in which we follow the ℓ identification derived from the period spacing analysis (see Table 11), and the other one to that shown in Table 13 (case 2), that corresponds to the identification assumed by Sullivan et al. (2008). We show our results in Figs. 19 and 20, where we display the inverse of the quality function for case 1 and case 2, respectively. Focusing on case 1, there is no good possible seismological solution in the range of effective temperatures allowed by spectroscopy, so we can adopt a relatively good fit model with $T_{\rm eff} = 26\,380$ K (slightly outside the allowed range of $T_{\rm eff}$) and $M_\star = 0.664\,M_\odot$, marked with a down arrow in Fig. 19. The nonexistence of a defined and clear seismological model in this case would indicate that

Table 12. Observed and theoretical periods of the asteroseismological solution for EC 20058 in the case 1, using 11 periods [$M_\star = 0.664\,M_\odot$, $T_{\rm eff} = 26\,380$ K].

$\Pi_i^{\rm O}$ (s)	$\ell^{\rm O}$	Π_k (s)	ℓ	k	m	$\delta\Pi_k$ (s)	$\dot{\Pi}_k$ (10^{-13} s/s)	Unstable
195.0	1	193.39	2	6	0	1.61	0.40	Yes
204.6	?	204.19	1	3	0	0.41	0.44	Yes
207.6	2	206.45	2	7	0	1.15	0.47	Yes
256.852	2	248.42	2	9	0	8.43	0.60	Yes
274.7	1	275.87	1	5	0	−1.17	0.53	Yes
280.983	2	275.87	1	5	0	5.11	0.53	Yes
286.6	?	293.03	2	11	0	−6.43	0.69	Yes
333.5	?	332.28	2	13	0	1.22	0.750	Yes
350.6	2	352.48	2	14	0	−1.88	0.62	Yes
525.4	1	524.05	1	12	0	1.35	1.11	Yes
539.8	?	538.01	2	23	0	1.79	1.24	Yes

Notes. Periods are in seconds and rates of period change (theoretical) are in units of 10^{-13} s/s. $\delta\Pi_i = \Pi_i^{\rm O} - \Pi_k$ represents the period differences, ℓ the harmonic degree, k the radial order, m the azimuthal index. The last column gives information about the pulsational stability/instability nature of the modes.

Table 13. Same as Table 12, but for case 2, in which eight periods are employed in the period fit.

$\Pi_i^{\rm O}$ (s)	$\ell^{\rm O}$	Π_k (s)	ℓ	k	m	$\delta\Pi_k$ (s)	$\dot{\Pi}_k$ (10^{-13} s/s)	Unstable
195.0	?	196.99	2	6	0	−1.99	0.29	Yes
204.6	1	208.24	1	3	0	−3.64	0.33	Yes
256.852	?	254.22	2	9	0	2.63	0.48	Yes
280.983	1	280.94	1	5	0	0.04	0.42	Yes
333.5	?	339.06	2	13	0	−5.56	0.54	Yes
350.6	?	349.46	1	7	0	1.14	0.43	Yes
525.4	?	526.18	2	22	0	−0.78	0.92	Yes
539.8	?	534.71	1	12	0	5.09	0.88	Yes

Notes. The possible asteroseismological solution for EC 20058 corresponds in this case to a DB WD model with $M_\star = 0.664\,M_\odot$, $T_{\rm eff} = 25\,467$ K.

the identification of the modes established in Table 11 based on possible period spacings with $\ell = 1$ and $\ell = 2$ could not be robust. In case 2, however, it is possible to find a small family of possible seismological solutions consisting of models with $M_\star = 0.664 M_\odot$ and $T_{\rm eff}$ in the range 25 000−26 000 K. In particular, there is a good asteroseismological solution for a model with $T_{\rm eff} = 25\,467$ K (marked with a down arrow in Fig. 20), well within the allowed range. Curiously, the mass of this seismological model is the same as that of the model with good period fit in case 1, although with a much lower effective temperature and in excellent agreement with the spectroscopic $T_{\rm eff}$ of EC 20058 ($T_{\rm eff} = 25\,500 \pm 500$ K). The theoretical periods of the models selected for case 1 and case 2 are included in Tables 12 and 13, along with the harmonic degree, the radial order, the difference with the observed periods, the rates of period change, and the pulsational stability nature of the modes. In particular, our identification of the harmonic degree and radial order of the modes for the asteroseismological solution of case 2 is remarkably similar to the identification of Sullivan et al. (2008; see their Table 5), even though those authors used DB WD models completely different than ours. Similar considerations hold when we compare the results of our case 2 with the results of Bischoff-Kim & Metcalfe (2011), even when they consider higher effective temperatures for EC 20058. A similar overall agreement between seismological results derived using the La Plata group evolution/pulsation models (using the LPCODE and LP-PUL numerical codes) and those from the Texas group (using the WDEC code) has been found in the case of the DBV pulsator WD 0158−160 (TIC 257459955), the first DBV studied with TESS (Bell et al. 2019). This agreement is encouraging, since the global asteroseismological results are not severely dependent on the WD modeling and period-fit methods used, which makes this type of analysis more robust.

We have also carried out period fits assuming that all the modes exhibited by EC 20058 are $\ell = 1$, but we have not found any possible seismological solution. Indeed, in general it is not possible with our models to reproduce the periods satisfactorily if they are considered as $\ell = 1$ only. This confirms that the pulsation spectrum of EC 20058 must be a mixture of dipole and quadrupole modes. Finally, we have tried leaving the identification free of all the modes (allowing them to be $\ell = 1$ or $\ell = 2$ from the outset). In this case, we find the same asteroseismological model as in case 2, although with a slightly poorer agreement between observed and theoretical periods.

In view of this analysis, we adopt the DB WD model with $M_\star = 0.664\,M_\odot$ and $T_{\rm eff} = 25\,467$ K, that corresponds to the best fit of periods of the case 2 (see Table 13), as the asteroseismological model for EC 20058. We obtain $\overline{\delta\Pi_i} = 2.61$ s, $\sigma = 3.22$ s, and BIC = 1.24. We show the characteristics of this model in Table 14. The internal chemical profiles and the

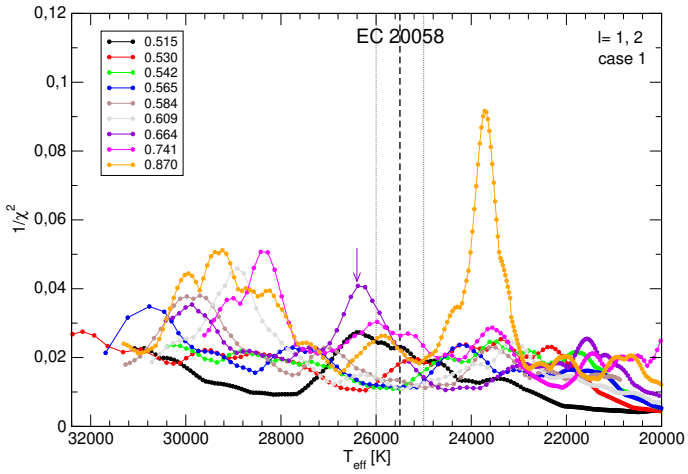

Fig. 19. Inverse of the quality function of the period fit in terms of the effective temperature, shown with different colors for the different stellar masses, corresponding to case 1 (11 periods). The vertical black dashed line corresponds to the spectroscopic $T_{\rm eff}$ of EC 20058 and the vertical dotted lines its uncertainties ($T_{\rm eff}$ = 25 500 ± 500 K; Koester et al. 2014). A local maxima (marked with an arrow), corresponds to a possible asteroseismological solution compatible with spectroscopy (see the text).

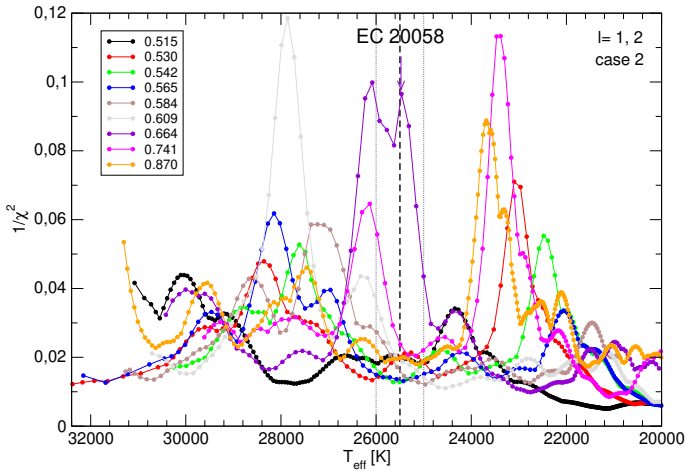

Fig. 20. Same as in Fig. 19, but for case 2, which involves eight periods. A clear maxima for a model with $T_{\rm eff}$ = 26 080 K and $M_\star = 0.664 M_\odot$, compatible with the spectroscopic effective temperature of EC 20058, is marked with an arrow (see the text).

Brunt-Väisälä and Lamb frequencies of this model are quite similar to those corresponding to the asteroseismological model of PG 1351 (Fig. 14). Indeed, the only difference between both models is the effective temperature ($\Delta T_{\rm eff} \sim 300$ K), which has a negligible impact on the chemical profiles and critical frequencies. Thus, Fig. 14 is also representative of the seismological model of EC 20058. We mention that the possible asteroseismological solution for case 1 is characterized by $\overline{\delta\Pi_i}$ = 2.77 s, σ = 3.74 s, and BIC= 1.34, which reflects that the period fit is worse than that of the adopted asteroseismological model (case 2). In addition, the model associated with the possible solution for case 1 is outside the range of the effective temperature allowed by spectroscopy.

Regarding the stability/instability of the modes of the asteroseismological model, we find that all the periods of EC 20058 are predicted to be excited according to our nonadiabatic computations, in line with the very existence of these oscillation periods in the spectrum of EC 20058 (see last column of Table 13). The same happens with regard to the possible seismological solution in case 1 (see last column of Table 12).

Table 14. Main characteristics of the DBV star EC 20058 according to the adopted asteroseismological model (case 2).

Quantity	Spectroscopy Astrometry	Asteroseismology
$T_{\rm eff}$ [K]	25 500 ± 500	25 467 ± 130
$M_\star$ [$M_\odot$]	0.614 ± 0.030	0.664 ± 0.013
$\log g$ [cm/s^2]	8.01 ± 0.05	8.062 ± 0.020
$\log(L_\star/L_\odot)$		−1.223 ± 0.03
$\log(R_\star/R_\odot)$		−1.901 ± 0.015
$(X_{\rm C}, X_{\rm O})_{\rm c}$		0.32, 0.65
$M_{\rm He}/M_\star$		5.42×10^{-3}
d [pc]	$117.95^{+0.68(a)}_{-0.75}$	$111.60^{+1.53}_{-1.50}$
π [mas]	8.48 ± 0.05$^{(a)}$	8.96 ± 0.12

References. (a) *Gaia* DR3.

Based on the asteroseismological model for EC 20058, we derive a seismological distance, as we did for PG 1351. We find a magnitude absolute in the *Gaia* photometry of M_G = 10.518 mag using a DB WD model atmosphere. Using the observed *Gaia* magnitude, m_G = 15.756 mag, we obtained $d_{\rm s} = 111.60^{+1.53}_{-1.50}$ pc. The seismological distance is ∼5% lower than the astrometric distance measured by *Gaia* EDR3, of $117.95^{+0.68}_{-0.75}$ pc, similar to we found for PG 1351.

5.3. EC 04207−4748

In Fig. 21, we schematically show for the DBV star EC 04207 the periods detected with TESS (upper panel), and the periods detected by Chote et al. (2013; lower panel). There are three common periods which are detected in both data sets (∼336 s, ∼423 s, and ∼447 s), and there is a period detected by Chote et al. (2013; ∼599 s) but not by TESS. In the case of the three periods that are common to both sets of data, we adopt for the asteroseismological analysis those detected by TESS as they are more precise. In summary, we have four periods in total to carry out the asteroseismological analysis. In the TESS data, the period of ∼423 s is actually a pair of periods very close to each other, of 423.882 s and 423.427 s. Assuming that they are the $m = -1$ and $m = +1$ component of a rotational triplet, the period corresponding to the central component (m = 0) is 423.655 s. We adopt this value of the period for this mode in the following analysis[5].

In Fig. 22 we show the statistical tests applied to the set of four periods in Table 15. The tests strongly suggest a possible constant period spacings of $\Delta\Pi \sim 21.9$ s. There is another possible period spacings at 17 s, 29 s, 37 s, and 43 s, that only are seen only in the K–S test, but not in the I–V test. To interpret these possible spacings of periods and assume an harmonic degree value for them, it is useful to first examine how they compare to the theoretical period-spacing values of stellar models. In other words, we can assign the values $\ell = 1$ or $\ell = 2$, or

[5] We have also considered the possibility that the periods of 423.882 s and 423.427 s are the $m = 0$ and $m = \pm 1$ components of a rotational triplet. The results we obtain in these cases are exactly the same as if we assume that the periods correspond to the components $m = +1$ and $m = -1$.

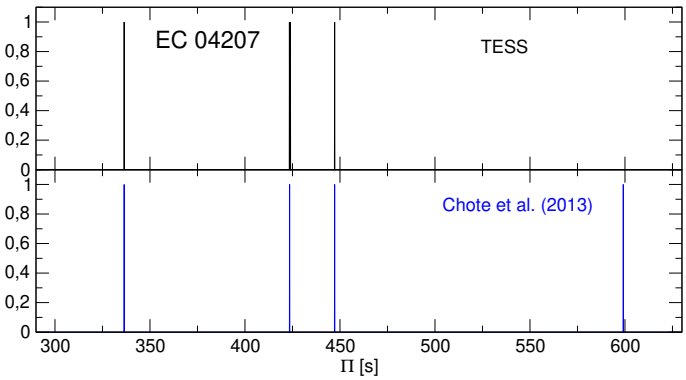

Fig. 21. Schematic distribution of the pulsation periods of EC 04207 according to TESS (3 periods, black lines, *upper panel*), and according to Chote et al. (2013; 4 periods, blue lines, *lower panel*). Actually, the period of ∼423 s from TESS is a couple of very similar periods, of 423.882 s and 423.427 s. The amplitudes have been arbitrarily set to one for clarity.

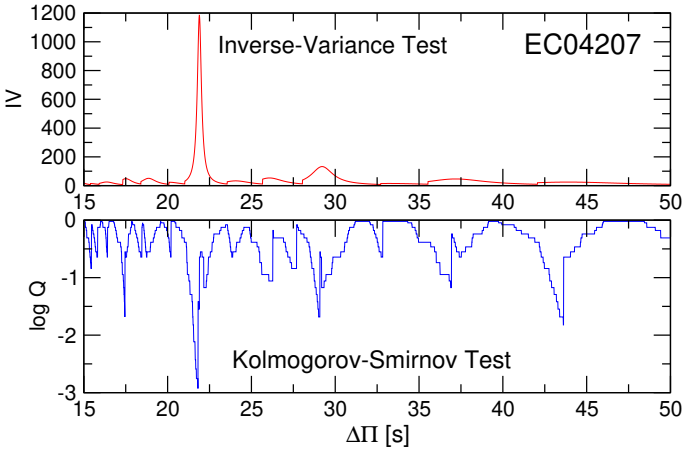

Fig. 22. I-V (*upper panel*) and K-S (*lower panel*) significance tests to search for a constant period spacing in EC 04207. The tests are applied to the set of 4 pulsation periods of Table 15, that includes the TESS plus Chote et al. (2013)'s periods. A period spacing of ∼38 s and its subharmonic of ∼19 s are evident.

Table 15. Enlarged list of periods of EC 04207.

Π_i^O (s) CEA13	Π_i^O (s) TESS	Π_{fit} (s)	$\delta\Pi$ (s)	ℓ^O
336.4	336.397	335.035	1.362	1
423.5	423.655			?
447.2	447.194	448.116	−0.922	1
599.1		598.891	0.209	1

Notes. Column 1 corresponds to four periods derived by Chote et al. (2013), and Col. 2 corresponds to the periods detected by TESS (Table 5). In the case of the couple of periods of TESS of 423.882 s and 423.427 s, we adopt a single value of 423.655 s (see the text).

simply rule out any indication of period spacing by plotting them together with the average of the theoretical period spacings in terms of effective temperature for different stellar masses. This is shown in Fig. 23, where we display the average of the computed period spacing $\overline{\Delta\Pi_k}$ (computed considering a period interval of 200−600 s) with curves of different colors to distinguish

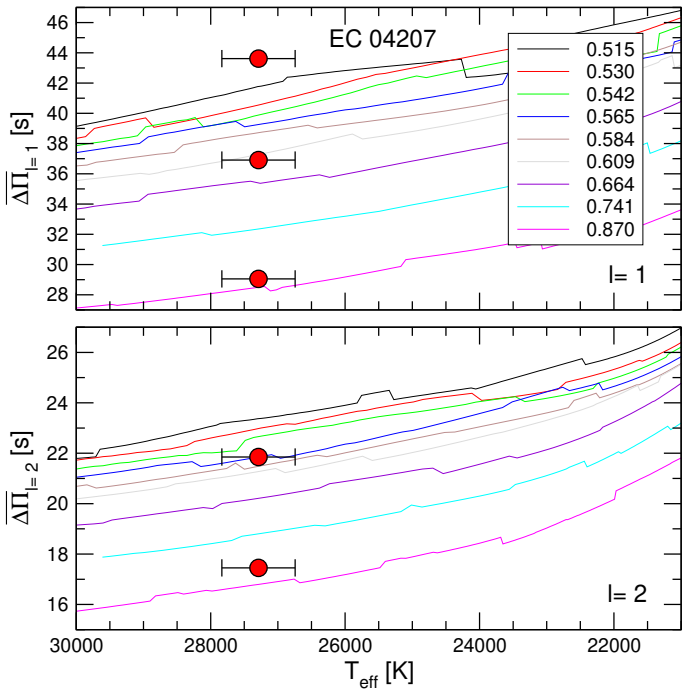

Fig. 23. *Upper panel*: Dipole ($\ell = 1$) average of the computed period spacings, $\overline{\Delta\Pi_k}$, assessed in a range of periods that includes the periods observed in EC 04207, shown as curves of different colors according to the different stellar masses. We consider the effective temperature $T_{\rm eff} = 27\,288 \pm 545$ K (Voss et al. 2007). *Lower panel*: Same as in *upper panel*, but for quadrupole ($\ell = 2$) modes. The red circles correspond to different possible period spacings as predicted by the statistical tests (see Fig. 22).

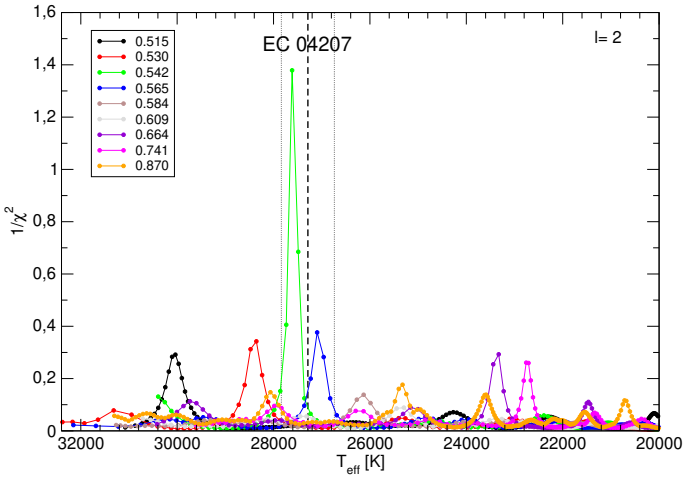

Fig. 24. Inverse of the quality function of the period fit with $\ell = 2$ in terms of the effective temperature, shown with different colors for the different stellar masses, corresponding to the four periods of EC 04207 in Table 15. The vertical black dashed line corresponds to the spectroscopic $T_{\rm eff}$ of EC 04207 and the vertical dotted lines its uncertainties ($T_{\rm eff} = 27\,288 \pm 545$ K; Voss et al. 2007). A prominent maxima corresponds to the best-fit model selected for EC 04207, with $M_\star = 0.542\,M_\odot$ and $T_{\rm eff} = 27\,614$ K.

the different stellar masses, corresponding to $\ell = 1$ (upper panel) and $\ell = 2$ (lower panel) modes. We note that the strongest peak in the statistical tests, that corresponds to $\Delta\Pi = 21.85$ s (averaging the values that arise from the K-S and I-V tests), must be associated with $\ell = 2$ modes, indicating a stellar mass of

$M_\star \sim 0.565\, M_\star$. The corresponding period spacing with $\ell = 1$ should be close to what the asymptotic theory predicts, that is 21.85 s $\times \sqrt{3} = 37.85$ s. Indeed, the peak at $\Delta\Pi = 36.91$ s in the K-S test is likely that dipole period spacing, indicating, in this case, a stellar mass of $M_\star \sim 0.609\, M_\odot$ for EC 04207. Alternatively, the presence of the possible period spacings at $\Delta\Pi = 17.45$ s ($\ell = 2$) and $\Delta\Pi = 29.05$ s ($\ell = 1$) would indicate a stellar mass of $M_\star \sim 0.82\, M_\odot$ and $M_\star \sim 0.85\, M_\odot$, respectively. Finally, the possible period spacing $\Delta\Pi = 43.62$ s, that should be associated with $\ell = 1$, would indicate a stellar mass too low ($M_\star \sim 0.50\, M_\odot$) and in contradiction with the indications of its spectroscopic parameters. Although all these possible period spacings are estimated on the basis of very few periods (four in total) – and therefore we cannot conclude anything definite regarding the stellar mass based on the period spacing – the strong signal of a possible period spacing of 21.85 s in both statistical tests would be indicating a stellar mass of $M_\star \sim 0.565 M_\star$. It remains to explain why the corresponding dipole period spacing period, of ∼37 s, appears not so noticeably and only in the K-S test. We have recomputed the K-S test for the cases in which we ignore the period of ∼424 s and the period of ∼447 s (one at a time). We still get the same strong indication of a ∼22 s period spacing in both cases. As for the possible dipole period spacing of ∼37 s, the associated minimum appears enhanced when we ignore the ∼ 424 s period, and remains unchanged when we ignore the ∼447 s period. We conclude that the ∼22 s period spacing is robust, and that the ∼37 s potential period spacing is sensitive to the presence or not of the ∼424 s period.

We have performed a period-to-period fit employing the four observed periods of EC 04207 from Table 15. We have fixed the harmonic degree $\ell = 2$ for all the periods, since they do fit the pattern of quadrupole period spacing derived above. The results of our period fit are shown in Fig. 24. The best fit corresponds to a model with a mass of $M_\star = 0.542\, M_\odot$ and an effective temperature $T_{\rm eff} = 27\,614$ K, compatible with the effective temperature of EC 04207. There is also another possible solution for $M_\star = 0.565\, M_\odot$ and $T_{\rm eff} = 27\,095$ K; although, the quality of the period match is poorer. We have repeated the analysis leaving free the harmonic degree of the four periods of EC 04207 (allowing them to be $\ell = 1$ or $\ell = 2$), that is, disregarding the constraints imposed by the period spacing derived above. In this case (not shown), we also find the same solution of $0.542\, M_\odot$ and $T_{\rm eff} = 27\,614$ K as before. We adopt the $0.542\, M_\odot$ model as the asteroseismological model for EC 04207. The average of the $\ell = 2$ period spacing for this model is $\overline{\Delta\Pi}_{\ell=2} = 22.09$ s, close to the period spacing derived from the statistical tests ($\Delta\Pi_{\ell=2} = 21.85$ s). A DBV pulsator with only $\ell = 2$ modes seems to be very unusual. In the case of DAVs, there is the ultra-massive ZZ Ceti star BPM 37094 that appears to be pulsating mostly with $\ell = 2$ modes (Metcalfe et al. 2004; Brassard & Fontaine 2005; Córsico et al. 2019b). As far as we are aware, there is no other DBV star with all its periods associated with $\ell = 2$ modes, apart from EC 04207 according to our analysis. It must be taken into account, however, that to put this result on a firmer basis, it would be necessary to detect more periods and, on the other hand, to carry out other independent asteroseismological analyses of EC 04207.

In Table 16 we show a comparison of the observed and theoretical periods and mode identifications, along with the theoretical rate of period change and stability nature of each mode. We get, for this model, $\overline{\delta\Pi_i} = 0.83$ s, $\sigma = 0.85$ s, and BIC= 0.16. We show the characteristics of this model in Table 17. The chemical composition profiles and the Brunt-Väisälä and Lamb frequencies of this model are displayed Fig. 25. We find that all the periods of EC 04207 are unstable according to our nonadiabatic computations, in line with the fact that we observe these oscillation periods in the pulsation spectrum of this star (see last column of Table 16).

Based on the asteroseismological model for EC 04207, we can assess a seismological distance, as we did for PG 1351 and EC 20058. We find a magnitude absolute in the *Gaia* photometry of $M_G = 10.126$ mag using a DB WD model atmosphere. Using the observed *Gaia* magnitude, $m_G = 15.229$ mag, we obtained $d_{\rm s} = 104.88^{+1.54}_{-1.94}$ pc. The seismological distance is ∼ 12% higher than the astrometric distance measured by *Gaia* EDR3, of $91.48^{+0.22}_{-0.23}$ pc. This discrepancy is an indication of the existence of uncertainties in the modeling of the interior of this DB WD star, and also of the scarcity of periods exhibited by this target, which make that the asteroseismological methods, in this case, lead to a seismological model that is not entirely well constrained.

We close this section by noting that, if instead of using the $T_{\rm eff} = 27\,288 \pm 545$ K of Voss et al. (2007) we used the effective temperature derived by Koester et al. (2014), that is $T_{\rm eff} = 25\,970 \pm 500$ K, the stellar mass suggested by the derived quadrupole period spacing of ∼19 s would be slightly higher, of $\sim 0.585\, M_\odot$ (as compared with $\sim 0.565\, M_\odot$). On the other hand, adopting the lower $T_{\rm eff}$ assessed by Koester et al. (2014) we could not find a seismological model for EC 04207.

5.4. WDJ152738.4-450207.4

This is a new DBV star discovered with the TESS data. The star exhibits five periods between ∼649 s and ∼746 s (Table 6). Three periods (701.754 s, 702.895 s, and 704.241 s) appear to be the components of a rotational triplet, suggesting a rotation period of $P_{\rm rot} \sim 2.3$ d. This rotation-period value is within what is usual to find in WDs (from 1 h to 4.2 d; see Kawaler 2015; Hermes et al. 2017a). The rotation period of ∼2.3 d is assessed by considering the *average* of the frequency splitting observed during the sector 38 of TESS, since clearly the frequency splittings are time dependent (for some unknown reason). In summary, we have only three independent pulsation periods (assumed to be $m = 0$ modes) of WD J1527 available from TESS for our asteroseismological analysis. If these periods were associated with low radial-order modes, they would be useful to establish strong asteroseismological constraints on the internal structure of WD J1527 (see, for example, the cases of the ZZ Ceti stars G226−29, G117−B15A, and R 548; Fontaine et al. 1992; Kepler et al. 1995; Bradley 1998). However, these three periods correspond to intermediate or high radial orders, lowering their asteroseismic potential. As we mentioned in Sect. 3.4, we acquired additional ground based observations in the hopes of increasing the number of detected periods. Observations with the 1.6 m OPD Telescope allowed us to find additional periods of 233.26 s, 352.93 s, 436.98 s, and 701.89 s. They complement the periods detected by TESS in such a way as to cover the short-period regime of the pulsation spectrum of the star. The addition of the short periods of 233.26 s, 352.93 s, 436.98 s enables an asteroseismological analysis. Since the period of 701.4 s detected from the ground corresponds to the rotationally triplet centered at 702.895 s, we do not take it into account in our period fit. First, we have searched for a uniform period spacing in the pulsational spectrum of WD J1527 by employing the statistical tests, but we did not find any conclusive result. Then, we performed a period-to-period fit, assuming that the period 702.895 s corresponds to a

Table 16. Observed and theoretical periods of the asteroseismological solution for EC 04207 [$M_\star = 0.542 M_\odot$, $T_{\rm eff} = 27\,614$ K].

$\Pi_i^{\rm O}$ (s)	$\ell^{\rm O}$	Π_k (s)	ℓ	k	$\delta\Pi_k$ (s)	$\dot{\Pi}_k$ (10^{-13} s/s)	Unstable
336.397	2	335.356	2	12	1.041	1.510	yes
423.655	2	422.653	2	16	1.002	1.594	yes
447.194	2	446.476	2	17	0.718	1.754	yes
599.100	2	599.646	2	24	−0.546	1.606	yes

Notes. Periods are in seconds and rates of period change (theoretical) are in units of 10^{-13} s/s. $\delta\Pi_i = \Pi_i^{\rm O} - \Pi_k$ represents the period differences, ℓ the harmonic degree, k the radial order, m the azimuthal index. The last column gives information about the pulsational stability/instability nature of the modes.

Table 17. Main characteristics of the DBV star EC 04207 according to the adopted asteroseismological model.

Quantity	Spectroscopy Astrometry	Asteroseismology
$T_{\rm eff}$ [K]	$27\,288 \pm 545$	$27\,614 \pm 100$
$M_\star$ [$M_\odot$]	0.515 ± 0.023	$0.542^{+0.017}_{-0.008}$
$\log g$ [cm s^{-2}]	7.808 ± 0.058	$7.872^{+0.027}_{-0.021}$
$\log(L_\star/L_\odot)$		-0.980 ± 0.008
$\log(R_\star/R_\odot)$		-1.850 ± 0.007
$(X_{\rm C}, X_{\rm O})_{\rm c}$		0.15, 0.83
$M_{\rm He}/M_\star$		1.32×10^{-2}
d [pc]	$91.48^{+0.22(a)}_{-0.23}$	$104.88^{+1.54}_{-1.94}$
π [mas]	$10.93 \pm 0.03^{(a)}$	$9.53^{+0.18}_{-0.13}$

References. (a) *Gaia* DR3.

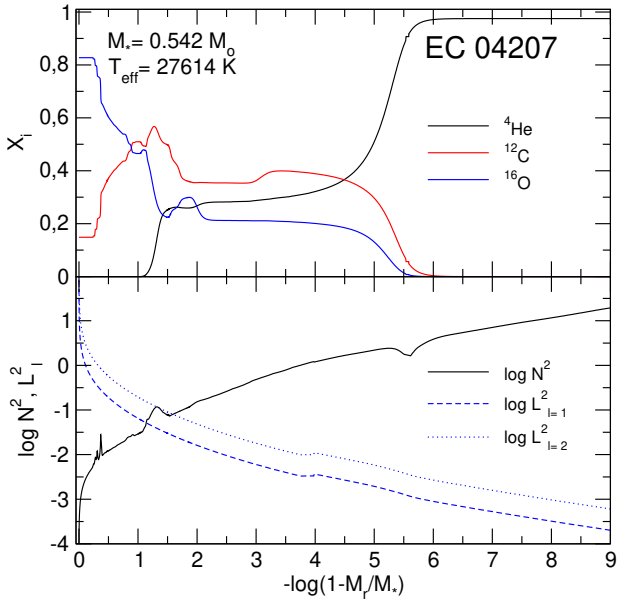

Fig. 25. Chemical profiles (*upper panel*) and the squared Brunt-Väisälä and Lamb frequencies for $\ell = 1$ and $\ell = 2$ (*lower panel*) corresponding to our asteroseismological DB WD model of EC 04207 with a stellar mass $M_\star = 0.542\,M_\odot$ and an effective temperature $T_{\rm eff} = 27\,614$ K.

mode with $\ell = 1$, $m = 0$ (the central component of a rotational triplet), and leaving free the value of ℓ for the other five periods (233.43 s, 352.48 s, 437.06 s, 649.397 s and 745.877 s). Our results for the inverse of the quality function versus the effective temperature for different stellar masses are shown in Fig. 26. There are several models that reproduce well the three periods of WD J1527, particularly a model with a stellar mass $M_\star = 0.609\,M_\odot$ at $T_{\rm eff} = 23\,658$ K. However, its effective temperature is not in good agreement with the spectroscopic effective temperature. Restricting ourselves to models that provide good agreement with the observed periods (local maxima of the inverse of χ^2) but at the same time satisfy the effective-temperature constraint, the best-fit model has $M_\star = 0.542\,M_\odot$ and $T_{\rm eff} = 25\,780$ K (green arrow in Fig. 26). We note that the mass of this model is substantially smaller than the spectroscopic mass of $M_\star = 0.675 \pm 0.022\,M_\odot$. In Table 18 we compare the observed pulsation periods of WD J1527 with the theoretical periods of this representative model and their ℓ and k values. The asymptotic period spacing of this model is $\Delta\Pi^{\rm a} = 42.107$ s. As we did for the other stars in this paper, we derive a seismological distance for WD J1527 using the $\log g$ and $T_{\rm eff}$ of the representative model. We find $d_{\rm s} = 111.98$ pc, that is about 20% larger than the *Gaia* astrometric distance, of 94.01 pc. Clearly, more observations of the WD J1527 variability from space and/or from the ground will be necessary to be able to analyze this DBV star in depth.

5.5. L 7−44

This is another new DBV star discovered with the TESS observations. Similarly to WD J1527, the TESS light curve of L 7−44 shows six independent periods, although three of them may belong to a rotational triplet, corresponding to a rotation period $P_{\rm rot} \sim 3.5$ d. This rotation period is within the expected range of WD rotation periods (Córsico et al. 2019a). The periods detected fall in the range 467 s−1019 s. Since all but one of the periods are quite long, and consequently they are in the asymptotic regime of pulsations of DBV stars, this set of periods is not potentially useful for a deep asteroseismological analysis. At variance with the case of WD J1527, for this star we do not have additional periods detected with observations from the ground available. With so few periods, for L 7−44 we limited ourselves to perform an exploratory asteroseismological analysis.

We first tried to find evidence of uniform period spacings, but we find no conclusive results and we ruled out the possibility of deriving a stellar mass through this approach. We also tried a period-to-period fit for this star. We considered the period of 914.955 s to correspond to a mode with $\ell = 1$, since it is likely the central component ($m = 0$) of a rotational triplet, being the other $m \neq 0$ components the periods 913.655 s and 916.436 s. Thus, we have four periods available for the period fit: 466.894 s, 914.955 s, 936.750 s, and 1019.138 s. We show in Fig. 27 the inverse of the quality function versus the effective temperature for different stellar masses, along with the location of L 7−44

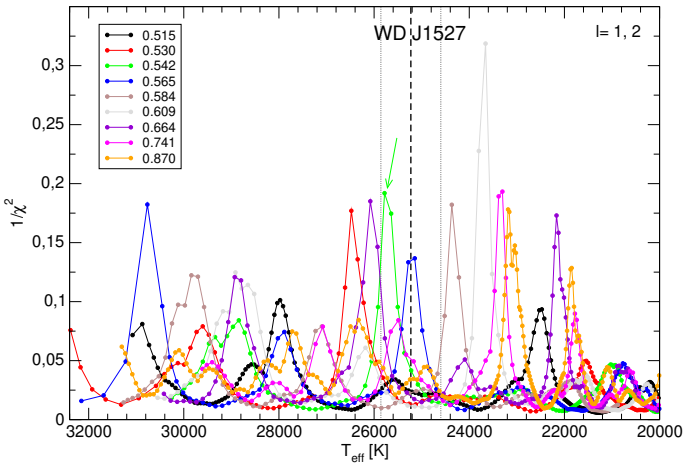

Fig. 26. Inverse of the quality function of the period fit in terms of the effective temperature, shown with different colors for the different stellar masses, corresponding to three of the five periods of WD J1527 in Table 6. The vertical black dashed line corresponds to the spectroscopic $T_{\rm eff}$ of WD J1527 and the vertical dotted lines its uncertainties ($T_{\rm eff}$ = 25 228 ± 630 K). A local maxima (marked with a green arrow), corresponds to a possible representative model for WD J1527 compatible with spectroscopy (see the text).

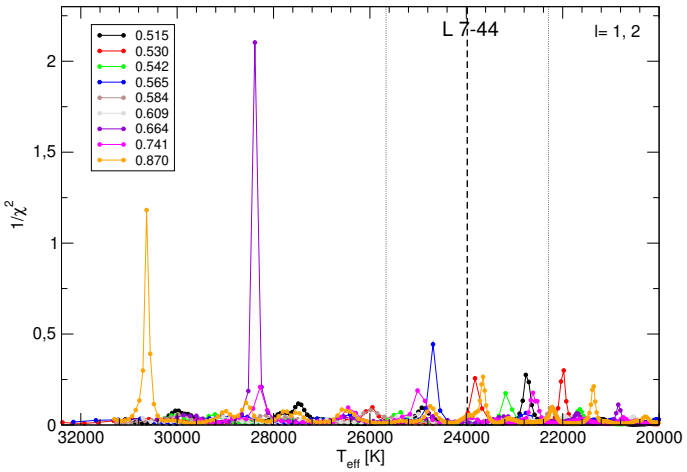

Fig. 27. Inverse of the quality function of the period fit in terms of the effective temperature, shown with different colors for the different stellar masses, corresponding to three of the five periods of L 7−44 in Table 8. The vertical black dashed line corresponds to the spectroscopic $T_{\rm eff}$ of L 7−44 and the vertical dotted lines its uncertainties ($T_{\rm eff}$ = 23 980 ± 1686 K; Rolland et al. 2018).

according to its effective temperature. There are two models that reproduce very well the periods of L 7−44, but they have very high effective temperatures. Among these two good fits, we have to discard that of $M_\star = 0.870\,M_\odot$ at $T_{\rm eff} = 30\,634$ K, because it corresponds to a model that is too massive and hot, in clear contradiction with the spectroscopic mass and the effective temperature of the star, $M_\star = 0.630\,M_\odot$ at $T_{\rm eff} = 23\,980 \pm 1686$ K. The other peak corresponds to a model with the stellar mass $M_\star = 0.664\,M_\odot$ at $T_{\rm eff} = 28\,387$ K, which provides the best agreement with the observed periods. In the range of effective temperatures allowed by spectroscopy, we find several small peaks associated with period fits of low quality. Among them, we consider that corresponding to a model with $M_\star = 0.565\,M_\odot$ and $T_{\rm eff} = 24\,690$ K, since it represents the best-fit model in the allowed interval of $T_{\rm eff}$. In Table 19 we show a comparison between the detected periods of L 7−44 and the theoretical periods of the model with $M_\star = 0.565\,M_\odot$ at $T_{\rm eff} = 24\,690$ K. The asymptotic period spacing of this model is $\Delta\Pi^{\rm a} = 42.07$ s. We derive a seismological distance for L 7−44 using the $\log g$ and $T_{\rm eff}$ of the representative model, and find $d_{\rm s} = 75.26$ pc, that is 9% larger than the *Gaia* astrometric distance, of 69.24 pc. As in the case of WD J1527, we emphasize that more short periods would be necessary before we can place significant constraints on the structure of L 7−44 with asteroseismology.

6. Summary and conclusions

In this paper, we presented an analysis of five pulsating DBV stars observed with the TESS mission. Three of the five analyzed targets are the already known DBV stars PG 1351, EC 20058, and EC 04207. The other two objects are new DBVs discovered with the TESS data: WD J1527 and L 7−44. With the discovery of these two new DBVs, the number of known stars of this class increases to 49. We examined the variability of these five DBV stars by analyzing their short and ultra-short-cadence single-sector observations obtained with TESS and found 18 significant independent oscillation frequencies.

We detected and measured just a single frequency and a combination frequency (the first harmonic of the independent frequency) for PG 1351 (see Table 3). In the case of EC 20058, we found two independent frequencies and no combination frequencies (Table 4). These two stars have very simple FTs, unlike the rest of the objects. Indeed, EC 04207, WD J1527, and L 7−44 have relatively rich FTs. Specifically, for EC 04207 we detected four independent frequencies along with three combination frequencies (Table 5), for WD J1527 we found five independent frequencies and one combination frequency (Table 6), and, finally, for L 7−44 we measured six independent frequencies and no combination frequencies (Table 8). In the case of WD J1527, we measured four additional independent frequencies from ground-based observations (Table 7). We also examined the running Fourier transform (sFT) of each target to investigate the temporal evolution of the pulsation modes. As in other compact pulsating stars, including sdBV, GW Vir, and DAV stars, we find variable amplitudes in the sFTs of WD J1527 (Fig. 8) and L 7−44 (Fig. 10). For two targets, EC 04207 and WD J1527, we estimated the possible rotation periods from g-mode frequency splittings. In the former case, the rotation period of EC 04207 would be either 1.14 or 2.28 d depending on the missing azimuthal order. We show in Fig. 6 the peaks corresponding to the frequencies at 2359.142 μHz and 2361.678 μHz which can be considered as two components of a rotationally split dipole mode. In the latter case, the rotation period of WD J1527 is constrained to 2.3 days. Figure 8 shows a detected rotational triplet with a splitting of ∼2.51 μHz for WD J1527. These findings are in line with what has been discovered for other types of pulsating WDs, such as GW Vir variables, the rotation periods of which ranges from 5 h to a few days (Córsico et al. 2019a, 2021; Uzundag et al. 2022), and DAV pulsating stars, for which it ranges from 1 h to 4.2 days (Kawaler 2015; Hermes et al. 2017a). According to the atmospheric parameters derived for WD J1527 from spectroscopic data, we found that the star is well within the DBV instability strip with an effective temperature of 25 228 K and surface gravity of 8.124 dex.

We also performed a detailed asteroseismological analysis of these stars on the basis of the fully evolutionary models of DB WDs computed by Althaus et al. (2009). In Table 20 we

Table 18. Observed and theoretical periods of the representative model of WD J1527 [$M_\star = 0.542\,M_\odot$, $T_{\rm eff} = 25\,780$ K].

$\Pi_i^{\rm O}$ (s)	$\ell^{\rm O}$	Π_k (s)	ℓ	k	$\delta\Pi_k$ (s)	$\dot{\Pi}_k$ (10^{-13} s/s)	Unstable
233.26	?	235.619	2	7	−2.189	0.927	Yes
352.93	?	351.457	2	12	1.023	1.340	Yes
436.98	?	440.544	2	16	−3.484	1.562	Yes
649.397	?	646.283	2	25	3.114	2.282	Yes
702.895	1	701.448	1	15	1.244	2.344	Yes
745.877	?	744.651	1	16	1.226	2.751	Yes

Notes. Periods are in seconds and rates of period change (theoretical) are in units of 10^{-13} s/s. $\delta\Pi_i = \Pi_i^{\rm O} - \Pi_k$ represents the period differences, ℓ the harmonic degree, k the radial order, m the azimuthal index. The last column provides information about the pulsational stability/instability nature of the modes.

Table 19. Observed and theoretical periods of a representative model of L 7−44 [$M_\star = 0.565\,M_\odot$, $T_{\rm eff} = 24\,690$ K].

$\Pi_i^{\rm O}$ (s)	$\ell^{\rm O}$	Π_k (s)	ℓ	k	$\delta\Pi_k$ (s)	$\dot{\Pi}_k$ (10^{-13} s/s)	Unstable
466.894	?	466.720	2	17	0.174	1.159	Yes
914.955	1	914.864	1	20	0.091	2.121	Yes
936.750	?	939.282	2	37	−2.532	2.358	Yes
1019.138	?	1017.539	2	40	1.599	2.902	Yes

Notes. Periods are in seconds and rates of period change (theoretical) are in units of 10^{-13} s/s. $\delta\Pi_i = \Pi_i^{\rm O} - \Pi_k$ represents the period differences, ℓ the harmonic degree, k the radial order, m the azimuthal index. The last column gives information about the pulsational stability/instability nature of the modes.

Table 20. Name of the studied stars (Col. 1), the independent periods detected with TESS (Col. 2), and the periods measured from ground-based observations (Col. 3).

Name	Periods from TESS [s]	Periods from ground-based observations [s]
PG 1351+489	**489.260**	**335.26**, 489.33, **584.68**, **639.63**
EC 20058	**256.852**, **280.983**	**195.0**, **204.6**, 207.6, 256.9, 274.7, 281.0, 286.6, **333.5**, **350.6**, **525.4**, **539.8**
EC 04207	**336.397**, **423.655**, **447.194**	336.4, 423.5, 447.2, **599.1**
WD J1527	**649.397**, 701.754, **702.895**, 704.241, **745.877**	**233.26**, **352.93**, **436.98**, 701.89
L 4−44	**466.894**, **914.955**, **936.750**, **1019.138**	

Notes. Periods in boldface are the ones used in the period-to-period fits (Sect. 5).

show the periods employed for the asteroseismological period fits of each target, including their origins (ground-based and TESS data). We summarize below our asteroseismological findings for each star:

- PG 1351: TESS detected only one period for this star, which agrees with one of the four periods detected from ground-based observations. We searched for a constant period spacing and found hints of a period spacing of ∼31 s for $\ell = 1$ modes and ∼19 s for $\ell = 2$ modes. These possible period spacings suggest a high mass for PG 1351, in the range 0.74−0.87 $M_\odot$. The period-to-period fit carried out on this star indicates an asteroseismological model with a stellar mass of $M_\star = 0.664 \pm 0.013\,M_\odot$, which is smaller than the mass indicated by the period spacings, although larger than the spectroscopic mass ($M_\star = 0.558 \pm 0.027\,M_\odot$).
- EC 20058: For this star, TESS detected only two periods, which are in perfect agreement with two of the 11 periods found from ground-based observations. The search for constant period spacings suggests the existence of a $\ell = 1$ period spacing of 41.4 s and a $\ell = 2$ period spacing of 23.8 s, which indicate a stellar mass of 0.53 $M_\odot$ and 0.55 $M_\odot$, respectively. According to this analysis, the 11 periods of EC 20058 are a mix of $\ell = 1$ and $\ell = 2$ periods, without rotational splitting multiplets present. An alternative analysis, proposed by Sullivan et al. (2008), consists of a period spectrum of both dipole and quadrupole periods, but with the presence of rotational triplets. A period-to-period fit analysis considering the above two possibilities results in the adoption of an asteroseismological model with a stellar mass of 0.664 $M_\odot$, which is substantially larger than the mass range indicated by the period spacings (0.53 $M_\odot$−0.55$M_\odot$) and in agreement with the spectroscopic mass of $M_\star = 0.614 \pm 0.030\,M_\odot$.
- EC 04207: For this star, TESS detected three periods, which are in agreement with three of the four periods detected from the ground. TESS failed to detect a period measured from ground-based telescopes (∼600 s). A search for a constant

Table 21. Name of the studied stars (Col. 1), the effective temperature and gravity of their asteroseismological or representative models (Cols. 2 and 3), the apparent and absolute *Gaia* magnitudes (Cols. 4 and 5), and the seismological and astrometric distances (Cols. 6 and 7).

Name	$T_{\rm eff}$ [K]	$\log g$ [cgs]	m_G [mag]	M_G [mag]	$d_{\rm s}$ [pc]	d_{Gaia} [pc]	Distance discrepancy
PG 1351+489	25 775	8.103	16.678	10.564	$167.05^{+2.31}_{-2.26}$	$175.73^{+1.53}_{-1.58}$	4.94 %
EC 20058−5234	25 467	8.062	15.756	10.518	$111.60^{+1.53}_{-1.50}$	$117.95^{+0.68}_{-0.75}$	5.38 %
EC 04207−4748	27 614	7.872	15.229	10.126	$104.88^{+1.54}_{-1.94}$	$91.48^{+0.22}_{-0.23}$	12.8 %
WD J1527−4502	25 780	7.877	15.482	10.236	111.98	$94.01^{+0.34}_{-0.37}$	16.0 %
L 7−44	24 690	7.921	14.737	10.354	75.26	$69.24^{+0.14}_{-0.12}$	8.0 %

Notes. Column 8 gives the discrepancy in the distances.

period spacing strongly suggests a $\ell = 2$ uniform period separation of ∼21.9 s, compatible with a stellar mass of $M_\star = 0.565\,M_\odot$. A period-to-period fit analysis for this star allowed us to find an asteroseismological model with a stellar mass of $0.542\,M_\odot$, which is somewhat higher than the spectroscopic mass ($0.515 \pm 0.023\,M_\odot$), but lower than the mass derived from the period spacing.

– WD J1527: This is one of the new DBV stars discovered with TESS. The star exhibits five periods between ∼649 s and ∼746 s, but three periods (701.754 s, 702.895 s, and 704.241 s) appear to be the components of a rotational triplet. We have also considered three additional periods (233.43 s, 352.48 s, and 437.0 s) detected with ground-based observations. We have not found a robust period spacing or a conclusive asteroseismological model. We have to wait for further observations of this star –either from space or from the ground– in order to analyze it in depth.
– L 7−44: This is the other new DBV star discovered with TESS. Similar to what happened in the case of WD J1527, L 7−44 exhibits six periods, three of which seem to be part of a rotational triplet. Thus, there are only four independent periods. Clearly, this is insufficient for asteroseismological modeling, so we are again limited to searching for a representative model that replicate the observed periods as closely as possible. For a deeper study, we will have to wait for new observations of the star.

We summarize in Table 21 the asteroseismological distances for the five stars analyzed in this work, and their comparison with their astrometric *Gaia* distances. We find a relatively good agreement (∼5−8%) between both sets of distance estimates for some stars (PG 1351, EC 20058, and L 7-44); although, for the cases of EC 04207 and WD J1527, the discrepancies are substantial (∼13−16%), meaning that the representative DB WD models used to estimate the distances are not entirely reliable.

The results presented in this work demonstrate that TESS currently has a great impact on the asteroseismology of WDs and pre-WDs –as well as in other classes of pulsating stars– as a worthy successor to the *Kepler*/K2 mission. We envisage that as this mission continues to provide uninterrupted high-quality photometric data of pulsating WD and pre-WDs, it will be possible to advance our understanding of the structure and evolution of these stars.

Acknowledgements. We wish to acknowledge the detailed suggestions and comments of an anonymous referee that strongly improved the original version of this work. This paper includes data collected with the TESS mission, obtained from the MAST data archive at the Space Telescope Science Institute (STScI). Funding for the TESS mission is provided by the NASA Explorer Program. STScI is operated by the Association of Universities for Research in Astronomy, Inc., under NASA contract NAS 5–26555. M.U. acknowledges financial support from CONICYT Doctorado Nacional in the form of grant number No: 21190886 and ESO studentship program. Part of this work was supported by AGENCIA through the Programa de Modernización Tecnológica BID 1728/OC-AR, and by the PIP 112-200801-00940 grant from CONICET. K.J.B. is supported by the National Science Foundation under Award AST-1903828. J.J.H. acknowledges support through TESS Guest Investigator Programs 80NSSC20K0592 and 80NSSC22K0737. Financial support from the National Science Centre under project No. UMO-2017/26/E/ST9/00703 is acknowledged. This research has made use of NASA's Astrophysics Data System.

References

Aerts, C. 2021, Rev. Mod. Phys., 93, 015001
Althaus, L. G., Serenelli, A. M., Panei, J. A., et al. 2005, A&A, 435, 631
Althaus, L. G., Panei, J. A., Miller Bertolami, M. M., et al. 2009, ApJ, 704, 1605
Althaus, L. G., Córsico, A. H., Isern, J., & García-Berro, E. 2010, A&ARv, 18, 471
Bailer-Jones, C. A. L., Rybizki, J., Fouesneau, M., Demleitner, M., & Andrae, R. 2021, VizieR Online Data Catalog: I/352
Baran, A. S., & Koen, C. 2021, Acta Astron., 71, 113
Battich, T., Althaus, L. G., & Córsico, A. H. 2020, A&A, 638, A30
Battich, T., Córsico, A. H., Althaus, L. G., & Miller Bertolami, M. M. 2016, J. Cosmol. Astropart. Phys., 8, 062
Beauchamp, A., Wesemael, F., Bergeron, P., et al. 1999, ApJ, 516, 887
Bédard, A., Bergeron, P., & Brassard, P. 2022, ApJ, 930, 8
Bell, K. J., Hermes, J. J., Bischoff-Kim, A., et al. 2015, ApJ, 809, 14
Bell, K. J., Hermes, J. J., Vanderbosch, Z., et al. 2017, ApJ, 851, 24
Bell, K. J., Córsico, A. H., Bischoff-Kim, A., et al. 2019, A&A, 632, A42
Bergeron, P., Wesemael, F., Dufour, P., et al. 2011, ApJ, 737, 28
Bischoff-Kim, A., & Metcalfe, T. S. 2011, MNRAS, 414, 404
Bischoff-Kim, A., Provencal, J. L., Bradley, P. A., et al. 2019, ApJ, 871, 13
Bognár, Z., Paparó, M., Córsico, A. H., Kepler, S. O., & Győrffy, Á. 2014, A&A, 570, A116
Bognár, Z., Kawaler, S. D., Bell, K. J., et al. 2020, A&A, 638, A82
Bohm, K. H., & Cassinelli, J. 1971, A&A, 12, 21
Borucki, W. J., Koch, D., Basri, G., et al. 2010, Science, 327, 977
Bradley, P. A. 1998, ApJS, 116, 307
Bradley, P. A. 2021, Front. Astron. Space Sci., 8, 229
Bradley, P. A., Winget, D. E., & Wood, M. A. 1993, ApJ, 406, 661
Brassard, P., & Fontaine, G. 2005, ApJ, 622, 572
Brickhill, A. J. 1991, MNRAS, 251, 673
Catelan, M., & Smith, H. A. 2015, Pulsating Stars (Wiley-VCH)
Chote, P., Sullivan, D. J., Montgomery, M. H., & Provencal, J. L. 2013, MNRAS, 431, 520
Clemens, J. C., Crain, J. A., & Anderson, R. 2004, SPIE Conf. Ser., 5492, 331
Córsico, A. H. 2020, Front. Astron. Space Sci., 7, 47
Córsico, A. H., & Althaus, L. G. 2006, A&A, 454, 863
Córsico, A. H., Althaus, L. G., & Miller Bertolami, M. M. 2006, A&A, 458, 259
Córsico, A. H., Althaus, L. G., Miller Bertolami, M. M., & García-Berro, E. 2009, J. Phys. Conf. Ser., 172, 012075
Córsico, A. H., Althaus, L. G., Miller Bertolami, M. M., & Bischoff-Kim, A. 2012, A&A, 541, A42
Córsico, A. H., Althaus, L. G., Miller Bertolami, M. M., Kepler, S. O., & García-Berro, E. 2014, J. Cosmol. Astropart Phys., 8, 054
Córsico, A. H., Althaus, L. G., Miller Bertolami, M. M., & Kepler, S. O. 2019a, A&ARv, 27, 7
Córsico, A. H., De Gerónimo, F. C., Camisassa, M. E., & Althaus, L. G. 2019b, A&A, 632, A119

Córsico, A. H., Uzundag, M., Kepler, S. O., et al. 2021, A&A, 645, A117
Córsico, A. H., Uzundag, M., Kepler, S. O., et al. 2022, A&A, 659, A30
Dalessio, J., Provencal, J. L., Sullivan, D. J., & Shipman, H. L. 2010, Am. Inst. Phys. Conf. Ser., 1273, 536
Dalessio, J., Sullivan, D. J., Provencal, J. L., et al. 2013, ApJ, 765, 5
Dehner, B. T., & Kawaler, S. D. 1995, ApJ, 445, L141
Duan, R. M., Zong, W., Fu, J. N., et al. 2021, ApJ, 922, 2
Fontaine, G., & Brassard, P. 2008, PASP, 120, 1043
Fontaine, G., Brassard, P., Bergeron, P., & Wesemael, F. 1992, ApJ, 399, L91
Fujimoto, M. Y. 1977, PASJ, 29, 331
Gentile Fusillo, N. P., Tremblay, P.-E., Gänsicke, B. T., et al. 2019, MNRAS, 482, 4570
Guidry, J. A., Vanderbosch, Z. P., Hermes, J. J., et al. 2021, ApJ, 912, 125
Hermes, J. J., Gänsicke, B. T., Kawaler, S. D., et al. 2017a, ApJS, 232, 23
Hermes, J. J., Kawaler, S. D., Bischoff-Kim, A., et al. 2017b, ApJ, 835, 277
Herwig, F., Blöcker, T., Langer, N., & Driebe, T. 1999, A&A, 349, L5
Howell, S. B., Sobeck, C., Haas, M., et al. 2014, PASP, 126, 398
Iben, I. J., Kaler, J. B., Truran, J. W., & Renzini, A. 1983, ApJ, 264, 605
Jenkins, J. M., Twicken, J. D., McCauliff, S., et al. 2016, Proc. SPIE, 9913, 99133E
Kawaler, S. D. 1988, IAU Symp., 123, 329
Kawaler, S. D. 2015, ASP Conf. Ser., 493, 65
Kepler, S. O. 1993, Baltic Astron., 2, 515
Kepler, S. O., Giovannini, O., Wood, M. A., et al. 1995, ApJ, 447, 874
Kepler, S. O., Pelisoli, I., Koester, D., et al. 2015, MNRAS, 446, 4078
Kepler, S. O., Pelisoli, I., Koester, D., et al. 2016, MNRAS, 455, 3413
Kepler, S. O., Pelisoli, I., Koester, D., et al. 2019, MNRAS, 486, 2169
Kilkenny, D., O'Donoghue, D., Crause, L. A., Hambly, N., & MacGillivray, H. 2009, MNRAS, 397, 453
Kleinman, S. J., Kepler, S. O., Koester, D., et al. 2013, ApJS, 204, 5
Koen, C., & Laney, D. 2000, MNRAS, 311, 636
Koen, C., O'Donoghue, D., Stobie, R. S., Kilkenny, D., & Ashley, R. 1995, MNRAS, 277, 913
Koester, D. 2010, Mem. Soc. Astron. It., 81, 921
Koester, D., & Kepler, S. O. 2015, A&A, 583, A86
Koester, D., Provencal, J., & Gänsicke, B. T. 2014, A&A, 568, A118
Kurtz, D. W. 2022, ARA&A, 60, 31
Landolt, A. U. 1968, ApJ, 153, 151
Lauer, A., Chatzopoulos, E., Clayton, G. C., Frank, J., & Marcello, D. C. 2019, MNRAS, 488, 438
Lenz, P., & Breger, M. 2005, Commun. Asteroseismol., 146, 53
Lightkurve Collaboration (Cardoso, J. V. d. M., et al.) 2018, Astrophysics Source Code Library [record ascl:1812.013]
Metcalfe, T. S., Montgomery, M. H., & Kanaan, A. 2004, ApJ, 605, L133
Miller Bertolami, M. M., & Althaus, L. G. 2006, A&A, 454, 845
Montgomery, M. H., Hermes, J. J., Winget, D. E., Dunlap, B. H., & Bell, K. J. 2020, ApJ, 890, 11
Nather, R. E., Winget, D. E., Clemens, J. C., Hansen, C. J., & Hine, B. P. 1990, ApJ, 361, 309
O'Donoghue, D. 1994, MNRAS, 270, 222
Østensen, R. H., Bloemen, S., Vučković, M., et al. 2011, ApJ, 736, L39
Rauch, T., Reiff, E., Werner, K., et al. 2006, ASP Conf. Ser., 348, 194
Redaelli, M., Kepler, S. O., Costa, J. E. S., et al. 2011, MNRAS, 415, 1220
Ricker, G. R., Winn, J. N., Vanderspek, R., et al. 2015, J. Astron. Telescopes Instrum. Syst., 1, 014003
Rolland, B., Bergeron, P., & Fontaine, G. 2018, ApJ, 857, 56
Romero, A. D., Kepler, S. O., Hermes, J. J., et al. 2022, MNRAS, 511, 1574
Schoenberner, D. 1979, A&A, 79, 108
Sullivan, D. J. 2003, NATO ASIB Proc. 105: White Dwarfs, 105, 231
Sullivan, D. J. 2005, ASP Conf. Ser., 334, 495
Sullivan, D. J. 2017, ASP Conf. Ser., 509, 315
Sullivan, D. J., Metcalfe, T. S., O'Donoghue, D., et al. 2008, MNRAS, 387, 137
Sullivan, D. J., Metcalfe, T. S., O'Donoghue, D., et al. 2007, ASP Conf. Ser., 372, 629
Tassoul, M., Fontaine, G., & Winget, D. E. 1990, ApJS, 72, 335
Unglaub, K., & Bues, I. 2000, A&A, 359, 1042
Unno, W., Osaki, Y., Ando, H., Saio, H., & Shibahashi, H. 1989, Nonradial Oscillations of Stars (Tokyo: University of Tokyo Press), 2nd ed.
Uzundag, M., Córsico, A. H., Kepler, S. O., et al. 2021, A&A, 655, A27
Uzundag, M., Córsico, A. H., Kepler, S. O., et al. 2022, MNRAS, 513, 2285
Van Grootel, V., Fontaine, G., Brassard, P., & Dupret, M. A. 2017, ASP Conf. Ser., 509, 321
Vanderbosch, Z. P., Hermes, J. J., Winget, D. E., et al. 2022, ApJ, 927, 158
Vincent, O., Bergeron, P., & Lafrenière, D. 2020, AJ, 160, 252
Voss, B., Koester, D., Napiwotzki, R., Christlieb, N., & Reimers, D. 2007, A&A, 470, 1079
Webbink, R. F. 1984, ApJ, 277, 355
Winget, D. E., & Kepler, S. O. 2008, ARA&A, 46, 157
Winget, D. E., Robinson, E. L., Nather, R. D., & Fontaine, G. 1982a, ApJ, 262, L11
Winget, D. E., van Horn, H. M., Tassoul, M., et al. 1982b, ApJ, 252, L65
Winget, D. E., van Horn, H. M., Tassoul, M., Hansen, C. J., & Fontaine, G. 1983, ApJ, 268, L33
Winget, D. E., Nather, R. E., & Hill, J. A. 1987, ApJ, 316, 305
Winget, D. E., Nather, R. E., Clemens, J. C., et al. 1994, ApJ, 430, 839
Winget, D. E., Sullivan, D. J., Metcalfe, T. S., Kawaler, S. D., & Montgomery, M. H. 2004, ApJ, 602, L109
York, D. G., Adelman, J., Anderson, J. E., Jr, et al. 2000, AJ, 120, 1579